Incorporation of diffuse interface in smoothed particle hydrodynamics: Implementation of the scheme and case studies

A. K. Das and P. K. Das*,†

Department of Mechanical Engineering, Indian Institute of Technology, Kharagpur 721302, India

SUMMARY

An algorithm is proposed to incorporate diffuse interface (DI) modelling in the Lagrangian smoothed particle hydrodynamics (SPH) for the simulation of interface and its evolution. The model assumes a smooth variation of properties across the interface of two immiscible fluids. The conventional Cahn–Hilliard equation has been adopted to take care of the property variation across the DI. However, it has been recast to be compatible with the particle-based formulation. The momentum equation has also been modified to account for the surface energy. Three different case studies namely evolution of gas bubbles at submerged orifice, drop deformation in shear flow and deformation of droplets in parabolic flow have been selected for the application of DI-based SPH (DI-SPH) method of solution. For the sake of comparison the predictions have been made for all the cases by DI-SPH as well as by the basic SPH without incorporating DI. Results of these two simulations have been compared with those already reported in the literature. In all the cases DI-SPH shows a definite improvement in the prediction of the complex interface and their dynamics. The present work demonstrates the strength of the technique in the simulation of diverse multiphase flow problems with evolving interfaces. Copyright © 2010 John Wiley & Sons, Ltd.

1. INTRODUCTION

Modelling the interface between two fluids is a challenge to both theoretical and computational fluid dynamics. The interface is most often represented as a stretched surface of zero thickness separating two fluids at two different pressures. The pressure difference is balanced by a special force termed as surface tension [1]. Such a picture of interface emerged from the works of Young [2], Laplace [3] and Gauss [4] in the early part of 1800. Mathematically it is needed to impose suitable boundary conditions at the interface to simulate processes like capillarity. In contrast, to the 'sharp interface' described above, Poisson [5], Maxwell [6] and Gibbs [7] conceived the interface as a narrow region characterized by a smooth but rapid variation of physical properties between the bulk values of the two fluids. The later description of the zone intermediate to both the fluids is known as Diffuse Interface (DI). The concept of DI was substantiated further by Raleigh [8]. Van der walls [9] postulated the gradient theory for the interface and formulated a method for the prediction of interface thickness based on the equation of state. Finally, the constitutive law of capillary stress tensor was developed by Kerteweg [10] in terms of the spatial gradient of density.

---

*Correspondence to: P. K. Das, Department of Mechanical Engineering, Indian Institute of Technology, Kharagpur 721302, India.
†E-mail: pkd@mech.iitkgp.ernet.in

Many problems of fluid mechanics have been solved based on the classical approach of sharp interface [11–13]. In this approach the moving interface has been modelled as an evolving free boundary. Accordingly, various computational techniques have also been developed for the simulation of surface tension and for tracking the sharp interface. In some of these methodologies interface is reconstructed at each instant of time to ascertain sharp interface. Simplified Line Interface Calculation (SLIC) [14] is most common among those techniques which readjust the scheme of discretization using a simplified algorithm based on its neighbors. Over the years a number of special algorithms have been developed to simulate the interface and its dynamics. These algorithms were developed mainly in connection with the grid-based computation. Volume of fluid (VOF) method [15] uses suitable reconstruction algorithms in a eulerian system to maintain a sharp interface by defining volume fraction of each phases in each grid volume. Later on, Brackbill *et al.* [16] presented continuum surface force (CSF) model which uses the gradient of fluid cell to calculate the surface normal and its curvature. Level set (LS) method [17] is yet another technique which has been used successfully to ensure a very sharp interface. For Lagrangian system different colour markers (surface marker and volume marker) has been introduced to track the distinct interface and model the surface tension. Tryggvason and Unverdi [18] used colour for surface particles to track fluid–fluid interactions and employed a front tracking methodology to determine the evolution of the interface. On the other hand, Morris [19] used colour for all the volume particles and employed high-order advection scheme for the determination of sharp fluid–fluid interface. Francois and Shyy [20] used front tracking marker-chain method embedded in immersed boundary technique to efficiently model surface tension and contact angle even in a completely non-wettable surface. Recently, Popinet [21] combined adaptive mesh refinement method, VOF, CSF method and height function curvature estimation method in a common framework to model typical surface tension driven interfacial flows like capillary breakup of viscous jet.

The methodologies for modelling two phase flow described so far are associated with grid-based techniques of computation. Over the years parallel efforts have been made to develop computational algorithm which are particle based or meshfree. The application of particle-based formulation for the modelling of fluid flow problems is relatively recent. Such formulations are particularly lucrative for multiphase flow and for flow with free surface. As neighbouring immiscible fluids can be represented by particles of different identities the effort needed to track the interface is minimal. Smoothed Particle Hydrodynamics (SPH) is one such techniques which has been successfully used in various fluid flow problems, such as dam break [22], sloshing [23] and shock tube [24]. Parallelly, various modifications in the methodology are made to simulate problems, such as viscous flow [25] and free surface flow [22]. Libersky and Petschek [26] tackled symmetrical surface boundary condition by inserting ghost particles along and outside the solid boundary. Hoover and Hoover [27] modelled the incompressible flow as a slightly compressible flow and proposed an artificial equation of state. No slip condition is simulated [28] incorporating artificial velocity for boundary particles. Morris [19] simulates surface tension between two fluids of the same density and viscosity following CSF model. Colagrossi and Landrini [29] modelled two-dimensional interfacial flow with low density ratios using SPH methodology. They also proposed new form of artificial viscosities for improvement of the prediction. Tartakovsky and Meakin [30] modelled surface tension for two phase flow using a controlled interplay between the random pinning forces created by particle–particle interaction and gravitational forces acting over the particles. Density re-initialization approach across the interface has been proposed by Chen *et al.* [31] for multiphase flow problems having large density difference. Hu and Adams [32] proposed a novel constant density approach to handle flows of large density ratio. They have calculated half time step velocity and intermediate pressure to correct the full time step parameters. Grenier *et al.* [33] extended the models proposed by Colagrossi and Landrini [29] and Hu and Adams [32] based on Lagrangian variational principle which can take care of simultaneous presence of free surface and fluid–fluid interface. The recent book by Liu and Liu [34] provides a very extensive review of the subject as well as provides many illustrations of the applications.

The acid test of any technique for simulating two phase flow lies in its capability of treating the interface. Most of the grid-based techniques and almost all the particle-based formulation uses

the concept of sharp interface. DI presents an alternative approach. This approach is based on a rigorous conservation of energy. Where the length scale of the phenomena is comparable to the interfacial thickness (for example near the critical point) DI gives a definite advantage over the free boundary description of interface. Besides, this method has been reported to give better results for contact line problems and complex topological problems, such as breakup and coalescence [35]. DI also helps to alleviate the numerical difficulties associated with stress singularities [36]. This has motivated the researchers to apply DI modelling for a multitude of problems.

The concept of DI is employed by researchers to address the interface between two immiscible fluids. Cahn and Hilliard [37] thermodynamically proved that local effect of free energy is not only dependent on its own composition, but also it is biased by its immediate neighbours. Antanovskii [38] developed a rheological expression for binary fluids subjected to topological changes considering an interfacial layer between the fluids. Anderson and McFadden [35] modelled compressible adiabatic motion of a single component fluid near its critical point using DI. Later on, Jacqmin [39] investigated moving contact line dynamics of a Cahn–Hilliard–van der Waals (CHW) mean field DI. His analysis of DI is utilized in both linearized and non-linear finite difference calculations. Liu and Shen [40] used coupled Navier–Stokes Cahn–Hilliard equation which includes energetic variational formulation for the extra stress representing the capillary effect of the mixture. Yue *et al.* [41] proposed DI approach for modelling of microstructured complex two phase system. Later on, they [42] have solved Cahn–Hilliard type convection diffusion equation using finite elements with adaptive meshing for simulation of interface dynamics of non-Newtonian fluids. Khatavkar *et al.* [43] used DI modelling by a combination of finite and spectral element methods for modelling of droplet impact over a smooth, flat, chemically homogeneous solid surface. Tapia and Lopez [44] proposed a free energy-based formulation of diffuse fluid–fluid–solid interface. van der Sman and van der Graaf [45] employed DI scheme in lattice Boltzmann equation for solving drop spreading phenomena in a shear flow field. They have also showed that artificial compressibility error induced by DI formulation can be eliminated by including surface tension as a body force in the Navier–Stokes equation.

For capturing the evolving interfaces, particle-based SPH eliminates some of the numerical complicacies involved in established methodologies, such as VOF, LS, CSF, BIM and their variants and combinations. On the other hand, DI is better suited to simulate complex interface structure and is more immune to stress singularities. It is expected that a combination of both the techniques can lend their individual advantages and provide an efficient and accurate description of the interface. But till date little effort has been made to incorporate DI in particle-based techniques due to its Lagrangian nature. Recently, Xu *et al.* [46] used mass density as ordered parameter to combine DI concept with SPH and investigated precipitation and dissolution problem of multiphase flow. But their model does not introduce separate transport equation for the order parameter. This leaves a scope for systematic development of a hybrid model incorporating DI concept in particle-based methodologies.

In the present paper, we have proposed that the sharp interface in a particle-based simulation for two phase flow can also be replaced by a zone of finite thickness and incorporated DI technique in SPH methodology as an extension. Developed methodology can efficiently model complex interfaces with high accuracy which cannot be predicted well with the existing models. In the next segment we discussed about the basic SPH formulation in brief and introduced DI modelling in particle-based formulation. In the third segment we have simulated three different dynamic interfacial problems using the developed methodology. It has been shown that DI-based methodology performs better in comparison with the sharp interface formulation of SPH.

2. MODEL DEVELOPMENT

A brief description of the Lagrangian particle-based SPH model has been discussed first in the following segment. Later on, improvisation for DI in the methodology has been reported and a combined DI-SPH technique has been developed.

2.1. The basic SPH model

The basic idea of SPH [47] is to discretize the domain of interest into a number of ordered particles having mass m_i, velocity v_i and density ρ_i. Absence of any physical connectivity between the particles makes the domain meshfree. Evolution of velocity, density or other thermophysical properties for a particle depends on the weighted average of the same of its neighbours. The zone of influence of a particle is determined by its smoothing length, h. Following steps are to be incorporated for the application of the above description in two phase flow systems.

Variable properties are estimated by field function approximation using an integral representation method commonly termed as kernel approximation. Mathematically,

$$f(x) = \int_\Theta f(x')W(x-x',h)\mathrm{d}x' \tag{1}$$

where $W(x-x',h)$ is the smoothing function having both unity property and delta function property [34]. Next, particle approximation is made which converts the integral equation into summations over all the neighboring particles. The particle approximation for a function at particle i can be written as:

$$f(x_i) = \sum_{j=1}^{N} \frac{m_j}{\rho_j} f(x_j)W\left(x_i-x_j, \frac{h_i+h_j}{2}\right) \tag{2}$$

Here, N is the number of particles of similar identity falling in the domain of smoothing length.

The error involved in approximating the function $f(x)$ by the summation is generally of second order or better. The main advantage of the method is that spatial derivative of a function can be easily estimated by transferring the derivative over the kernel function. Following the same argument, nth derivative of a function $f(x)$ can be written as:

$$\nabla^n.f(x_i) = -\sum_{j=1}^{N} \frac{m_j f(x_j)}{\rho_j} \nabla^n.W\left(x_i-x_j, \frac{h_i+h_j}{2}\right) \tag{3}$$

As the particle approximation introduces mass and density of the particle into the equation, the hydrodynamic problems where density is a key parameter, can be modelled readily using this methodology. Particulate nature of the domain helps to calculate the density field without solving the mass conservation equation. This is termed as summation density approach and is expressed as [48]:

$$\rho_i = \frac{\sum_{j=1}^{N} m_j W_{ij}}{\sum_{j=1}^{N} \left(\dfrac{m_j}{\rho_j}\right) W_{ij}} \tag{4}$$

Using kernel approximation and particle approximation momentum equation for the continuum reduces into the following form:

$$\frac{\mathrm{D}v_i^\alpha}{\mathrm{D}t} = \sum_{j=1}^{N} m_j \left(\frac{\sigma_i^{\alpha\beta}+\sigma_j^{\alpha\beta}}{\rho_i \rho_j} + \pi_{ij}\right)\frac{\partial W_{ij}}{\partial x_i^\beta} \tag{5}$$

or

$$\frac{\mathrm{D}v_i^\alpha}{\mathrm{D}t} = \sum_{j=1}^{N} m_j \left(\frac{\sigma_i^{\alpha\beta}}{\rho_i^2}+\frac{\sigma_j^{\alpha\beta}}{\rho_i^2} + \pi_{ij}\right)\frac{\partial W_{ij}}{\partial x_i^\beta} \tag{6}$$

where

$$\sigma_i^{\alpha\beta} = -p_i \delta^{\alpha\beta} + \mu_i \left(\frac{\partial v_i^\beta}{\partial x_i^\alpha}+\frac{\partial v_i^\alpha}{\partial x_i^\beta} - \frac{2}{3}(\nabla v_{ij})\delta^{\alpha\beta}\right)$$

In the above formulation, v_i^α is the absolute velocity of particle i and p_i is the pressure of particle i. For calculating the Neumann–Richtmyer artificial viscosity π_{ij} Monaghan [49] related particle distribution with the viscosity in the following manner:

$$\pi_{ij} = \begin{cases} \dfrac{-(c_i + c_j) \sum_j \dfrac{h v_{ij} x_{ij}}{x_{ij}^2 + \eta^2} + 2 \left(\sum_j \dfrac{h v_{ij} x_{ij}}{x_{ij}^2 + \eta^2} \right)^2}{\rho_i + \rho_j} & \text{for } v_{ij}.x_{ij} < 0 \\ 0 & \text{for } v_{ij}.x_{ij} \geqslant 0 \end{cases} \tag{7}$$

where $\eta^2 = 0.001 h^2$, v_{ij} and x_{ij} is the relative velocity and distance of two particles i and j Smoothing length (h) is an important parameter as it controls the accuracy and computational efficiency of the simulation. It is, therefore, necessary to dynamically evolve h to ensure unity property of the smoothing function. Benz [50] suggested a methodology which correlates change of smoothing length with dynamic density. In the present paper we have followed the same criteria as depicted in Equation (8).

$$\frac{dh_i}{dt} = -\frac{1}{2} \frac{h_i}{\rho_i} \frac{d\rho_i}{dt} \tag{8}$$

An iterative solver for the values of h and ρ using Equation (4) and (8) is used. A $\pm 0.5\%$ criterion is used for the convergence in all the case studies.

To maintain a quasi-compressible state for the fluids a relationship between the particle density and fluid pressure is necessary. The following relationship has been used following Monaghan [22] correlation:

$$p_i = B \left(\left(\frac{\rho_i}{\rho_0} \right)^f - 1 \right) \tag{9}$$

Here ρ_0 is the reference density measured at the atmospheric pressure. Value of f and B are 7 and 3.04×10^8, respectively, as suggested by Liu et al. [51].

The present model further assumes that there is no surface irregularity of the solid surface and it is perfectly smooth. At the solid boundary two additional layers of particles are placed to impose impermeability. These particles pose a resistive force to the interior particles. A Lennard-Jones [52] type force is assumed to ensure no slip and no penetration condition at the solid fluid boundary. The expression for resistive force is as follows:

$$F(R) = D \left[\left(\frac{r_0}{r_{ij}} \right)^{12} - \left(\frac{r_0}{r_{ij}} \right)^6 \right] \frac{x_{ij}}{r_{ij}^2} \quad \text{for } r_{ij} \langle r_0$$

$$= 0 \quad \text{for } r_{ij} \geqslant r_0 \tag{10}$$

Here, r_{ij} is the scalar distance between the boundary particle and the fluid particle. r_0 is the minimum spacing of the particles. D is assumed to be $15\,g$ times the initial spacing of the particles. Similar treatment has also been applied for the interface to avoid an abrupt mixing of the phases. The time step is determined so that the physical rate of propagation of information to be less than that of the numerical propagation rate. Moreover, an additional diffusive limitation is imposed on the time step and the two effects are usually combined in the following expression:

$$\Delta t = \min_i \frac{h_i}{c_i + 0.6(\alpha_c c_i + \beta_c \max_j \mu_{ij})} \tag{11}$$

Values of α_c and β_c are reported in Liu and Liu [34]. Simulation is forward marched with the proposed time step using second-order predictor corrector scheme. Cubic spline is considered as a kernel function for particle to particle interaction. 'All pair search algorithm' [34] is used to identify the immediate neighbours of a particle under consideration.

Surface tension force is applied in the momentum equation as a source term. CSF method has been applied to calculate force per unit volume, F_s, which follows the following equation:

$$F_{si} = f_{si}\delta_s \tag{12}$$

Here δ_s is the delta function which is unity only at the interface and zero elsewhere. f_s is the force per unit area. A colour attribute C_s is set to 1 for liquid phase and 0 for gaseous phase. Following the idea of Morris [19, 53] surface tension forces per unit area can be computed as:

$$f_{si} = -\sigma_{\mathrm{lg}} \sum_{j=1}^{N} \frac{m_j}{\rho_i \rho_j} \frac{(C_i - C_j)}{|r_{ij}|} \frac{\partial^2 W_{ij}}{\partial r_{ij}^2} \frac{n_s}{|n_s|} \tag{13}$$

Here, σ is the surface tension force along the normal direction of the interface n. n can be calculated as $n_s = \nabla C$. In the next segment DI concept has been recast in the basic formulation for improvement of the scheme while predicting complex dynamic interfaces.

2.2. Modification of present methodology

The schematic representation of both sharp and DI is shown in Figure 1. In this figure two different phases are represented by particles of white (phase I) and black (phase II) colour. The propagating sharp interface is characterized by a sudden jump of any thermophysical properties, say from f_1 to f_2 across a zero thickness of the phase boundary (Figure 1(a)–(b)). On the other hand, the change of properties across the finite thickness ξ of the DI is rapid but gradual (Figure 1(c)–(d)). Though the concept of DI is deeply rooted in thermodynamics suitable computational scheme is needed for its implementation. For the physical description of the phase boundary one may consider a surface with an average value of property $(f_1 + f_2)/2$. Figure 1 depicts the motion of the interface as conceived by both sharp interface and DI.

Van der Waals [54] first proposed the idea considering the free energy minimization concept. Historically, Cahn [55] extended the classical model of Van der Waals [54] for unsteady problems where movement of triple line is present. He correlated interfacial diffusion with the chemical potential gradient to track the mobility of the triple line. The governing differential equation for the interface is commonly known as Cahn–Hilliard equation. In the present work we have adopted Cahn–Hilliard equation for a particle-based system considering a finite thickness of the liquid–gas interface. Like other thermophysical properties of the fluids one colour code (C) has also been assigned to the fluid particles having $+1$ value for the liquid and -1 for the gas. Chemical potential of the fluid (Φ) is calculated based on the colour code near the interface around which a smooth transition of C is considered. ϕ is calculated for each phase as given below:

$$\phi = [\nabla(C+1)^2(C-1)^2 - (Cn^2\nabla^2 C)] \tag{14}$$

In the above, the first and the second parts of the RHS of Equation (14) signifies bulk energy ($\nabla\psi_c$) and phase gradient energy ($Cn^2\nabla^2 C$), respectively. ψ_c is a function $((C+1)^2 - (C-1)^2)$ which captures the immiscibility of the fluid pair having two minima at the corresponding bulk phases of the fluids. Cn is the Cahn number which is the ratio of mean interfacial thickness (ξ_i) and characteristic length (L_c). The characteristic length can be selected suitably depending on the problem and ξ is taken as $10\,\mu\mathrm{m}$. Value of ξ can be minimized further if the particle density is increased. Prediction of accurate Cahn number is very important for an effective simulation of the interface and the transport phenomena across it. It basically defines the interfacial thickness in case of DI assumption. After using kernel and particle approximations Equation (14) can be represented for the particle-based system in the following manner:

$$\phi_i = \sum_{j=1}^{N} \frac{m_j}{\rho_i \rho_j} \frac{((C_i+1)^2(C_i-1)^2 - (C_j+1)^2(C_j-1)^2)}{|r_{ij}|} \frac{\partial W_{ij}}{\partial r_{ij}}$$
$$- \sum_{j=1}^{N} \frac{m_j}{\rho_i \rho_j} \frac{(Cn_i^2 + Cn_j^2)(C_i - C_j)}{|r_{ij}|} \frac{\partial^2 W_{ij}}{\partial r_{ij}^2} \tag{15}$$
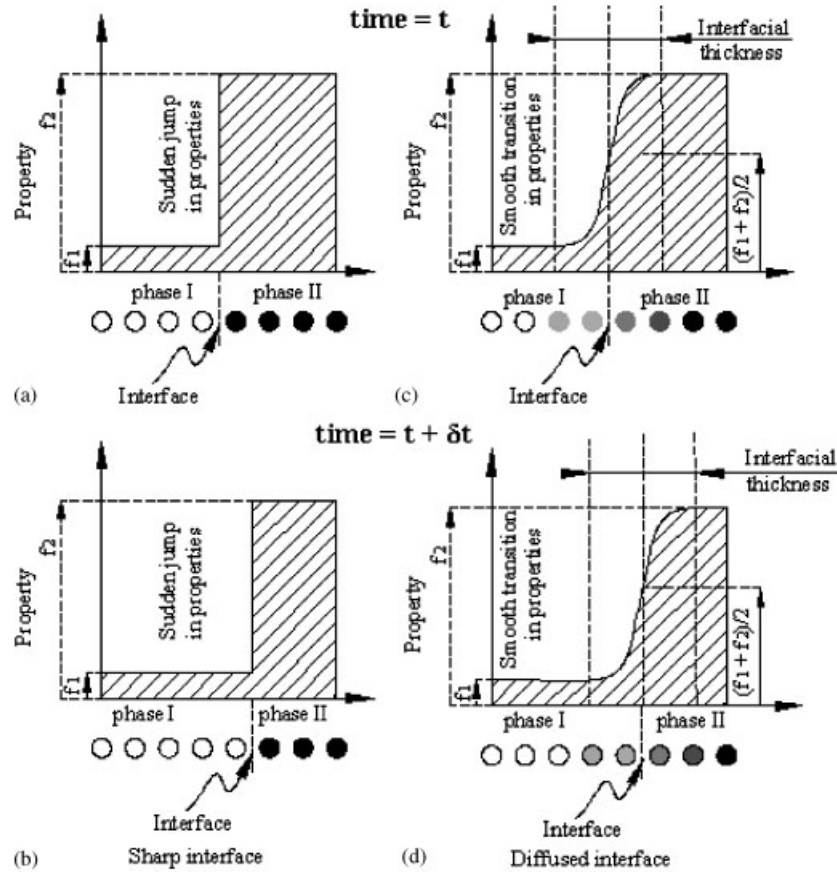
Figure 1. Scheme of DI concept in SPH.

One can derive the transport equation of C by approximating interfacial diffusion fluxes proportional to the chemical potential gradients:

$$\frac{\mathrm{D}C}{\mathrm{D}t} = k\nabla^2\phi \tag{16}$$

For the particle-based continuum conservation equation of C can be written in the following form:

$$\frac{\mathrm{d}C_i}{\mathrm{d}t} = \sum_{j=1}^{N} \frac{m_j}{\rho_i \rho_j} \frac{k(\phi_i - \phi_j)}{|r_{ij}|} \frac{\partial^2 W_{ij}}{\partial r_{ij}^2} \tag{17}$$

In Equation (15), k is the mobility [56, 57] and taken as 10^{-4} after detail optimization study without sacrificing numerical simplicity and accuracy. Increase or decrease in the value of mobility may deteriorate the predictability or increase the computational effort, respectively. As a physical thickness is assigned to the interface following the concept of DI, the momentum balance equations (Equations (5)–(6)) will change accordingly. After the incorporation of the source term to take care the interfacial free energy, the momentum equation can be written as follows [39]:

$$\rho \frac{\mathrm{D}\overline{v}}{\mathrm{D}t} = -\nabla p + \nabla \cdot \tau + \rho\overline{g}z - \frac{C}{CapCn}\nabla\phi \tag{18}$$

Using kernel [34] and particle approximations [34] momentum equation for the continuum reduces to:

$$\frac{\mathrm{D}v_i^\alpha}{\mathrm{D}t} = \sum_{j=1}^N m_j \left(\frac{\sigma_i^{\alpha\beta} + \sigma_i^{\alpha\beta}}{\rho_i \rho_j} + \pi_{ij} \right) \frac{\partial W_{ij}}{\partial x_i^\beta} - \sum_{j=1}^N \frac{m_j}{\rho_i \rho_j} \frac{\left(\dfrac{C_i}{Cap_i Cn_i} + \dfrac{C_j}{Cap_j Cn_j} \right)(\phi_i - \phi_j)}{|r_{ij}|} \frac{\partial W_{ij}}{\partial r_{ij}} \quad (19)$$

or

$$\frac{\mathrm{D}v_i^\alpha}{\mathrm{D}t} = \sum_{j=1}^N m_j \left(\frac{\sigma_i^{\alpha\beta}}{\rho_i^2} + \frac{\sigma_i^{\alpha\beta}}{\rho_i^2} + \pi_{ij} \right) \frac{\partial W_{ij}}{\partial x_i^\beta} - \sum_{j=1}^N \frac{m_j}{\rho_i \rho_j} \frac{\left(\dfrac{C_i}{Cap_i Cn_i} + \dfrac{C_j}{Cap_j Cn_j} \right)(\phi_i - \phi_j)}{|r_{ij}|} \frac{\partial W_{ij}}{\partial r_{ij}} \quad (20)$$

$\sigma_i^{\alpha\beta}$ is defined in Equation (6) and Cap is the particulate capillary number which is defined as follows:

$$Cap_i = \frac{2\sqrt{2}\mu_i u_i}{3\sigma_{\mathrm{lg}}} \quad (21)$$

Though SPH does not explicitly depend on the boundary following boundary conditions are set for the colour code to close the system. No flux condition for chemical potential is assumed at the interface and solid liquid contact plane, if any.

$$\sum_{j=1}^N \frac{m_j}{\rho_i \rho_j} \frac{(\phi_i - \phi_j)}{|r_{ij}|} \frac{\partial W_{ij}}{\partial r_{ij}} = 0 \quad (22)$$

Second boundary condition for the colour code proposed by Jacqmin [39] ensures that the interface at the triple line remains at the local equilibrium condition, if present. The boundary condition is as follows:

$$\sum_{j=1}^N \frac{m_j}{\rho_i \rho_j} \frac{(\phi_i - \phi_j)}{|r_{ij}|} \frac{\partial W_{ij}}{\partial r_{ij}} + \sum_{j=1}^N \frac{m_j}{\rho_i \rho_j} \left(\frac{3kw_i}{4Cn_i}(1 - C_i^2) - \frac{3kw_j}{4Cn_j}(1 - C_j^2) \right) = 0 \quad (23)$$

Second term of the LHS of Equation (20) signifies the local surface energy at a particular location. This equation diffusively controls local equilibrium at the fluid–fluid interface. In the above equation, kw is the wetting coefficient whose value equals to the cosine of the physical contact angle of the fluid solid pair. Density and viscosity of the particles in the interfacial region are calculated using simple mixture rule as follows:

$$\frac{1}{\rho_i} = \frac{1}{\rho|_{C_i=1}} \left(\frac{C_i + 1}{2} \right) - \frac{1}{\rho|_{C_i=0}} \left(\frac{C_i - 1}{2} \right) \quad (24)$$

and

$$\frac{1}{\mu_i} = \frac{1}{\mu|_{C_i=1}} \left(\frac{C_i + 1}{2} \right) - \frac{1}{\mu|_{C_i=0}} \left(\frac{C_i - 1}{2} \right) \quad (25)$$

Discretization of regions near the interface is handled with care to incorporate the DI concept. The particle spacing in the DI domain is reduced to half of the same imposed for the bulk fluids away from the interface. On the other hand, the particle spacing of the bulk phase has been selected through a rigorous test. To achieve the required accuracy the particle spacing of the bulk phase is continuously reduced till the present interfacial shape matches with the published result. It may be noted that there may be other schemes for selecting the particle spacing. However, the present scheme worked very well and produced very good agreement with experimental/theoretical results taken from different sources. During the evolution of the interfacial region the particle positions and the colour codes are continuously changed obeying Equation (17) and (15), respectively.
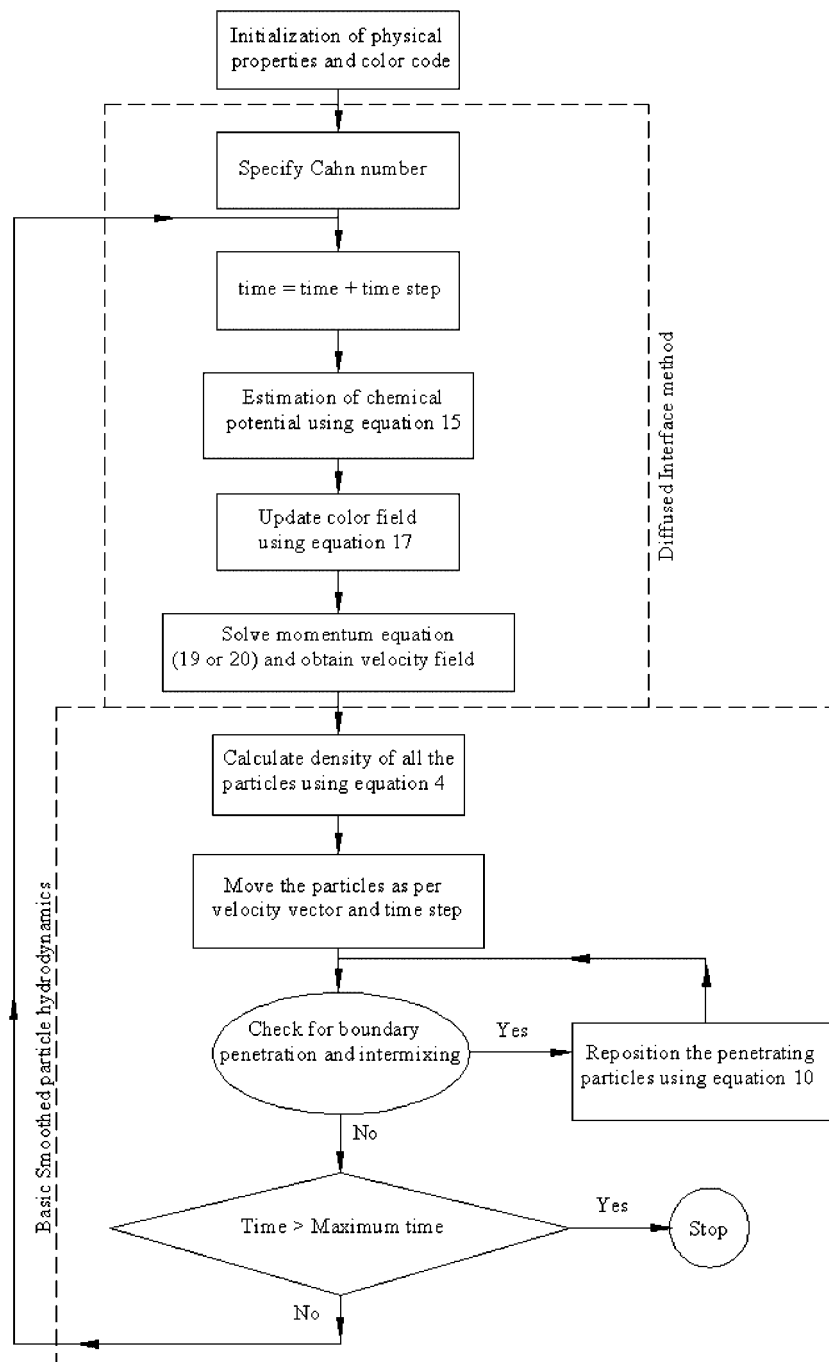
Figure 2. Algorithm for hybrid DI-SPH method.

Incorporation of DI methodology in the fluid–fluid interfaces inherently entered surface tension force in the momentum equation. Separate algorithm like CSF for surface tension force becomes insignificant under this situation. But for the sake of comparison between the basic and DI-based SPH we have applied CSF model in both the formulation. Separate investigation is needed to justify the application of CSF method along with the DI concept. An algorithm for hybrid DI-SPH formulation is shown in Figure 2.

3. NUMERICAL EXAMPLES

The previous section describes the modifications needed for the incorporation of DI in the basic algorithm of SPH. The modifications have been done in a generic manner so that the DI-SPH technique can be used to simulate a large variety of problems. Developed DI-SPH model is consistent for the prediction of complex interfaces. The developed technique has been put to test through three different case studies. The examples have been selected such that the properties of the two phases are grossly different and the interface experiences a complex evolution in profile due to the associated fluid dynamics. In all the examples the effect of interfacial tension is important and the success of simulation depends on its correct modelling. In one of the test cases buoyancy force (or the effect of gravity) plays an important role. Additionally, inertia and pressure driven flow situations have also been considered. All the problems have been simulated by both SPH and DI-SPH to examine the improvement in the prediction by the incorporation of the concept of DI in the basic SPH scheme. The results of these simulations have been compared with those already published in the literature.

3.1. Formation growth and departure of bubbles from a submerged orifice

Formation of gas bubbles at a submerged orifice, their evolution and finally their departure from the orifice mouth is important for industrial processes which involve aeration. Besides, due to the fundamental nature of the phenomenon, a volume of research activities have been conducted on this topic over last few decades. After the pioneering work of Davidson and Amick [58] numerous efforts have been made to study the phenomena through experiments and to simulate it by various models [59–65]. To start with analytical models were tried. In the early efforts instead of solving the full Navier–Stokes equation solution through force balance or momentum balance were sought. Kulkarni and Joshi [66] made a good review of the previous investigations on the formation of gas bubbles and their subsequent rise due to buoyancy. The efforts to model the process computationally are of recent origin. The main stumbling block for modelling the phenomena numerically rested in the treatment of the evolving interface. Initially, researchers tried to restore this issue using finite element or similar techniques. As a first attempt Oguz and Prosperetti [67] investigated the bubble formation at high flow rates using Boundary element method (BEM). Same procedure has been applied by Wong *et al.* [68] and Higuera [69] for bubble formation through a highly viscous liquid. Durst and co-workers [70–72] addressed various aspects of this problem.

All these techniques required a costly algorithm for interface construction in dynamic situations. Recently a Lagrangian particle-based methodology SPH has been used by Das and Das [53] for simulation of bubble evolution from a submerged orifice. The basic formulation of the methodology
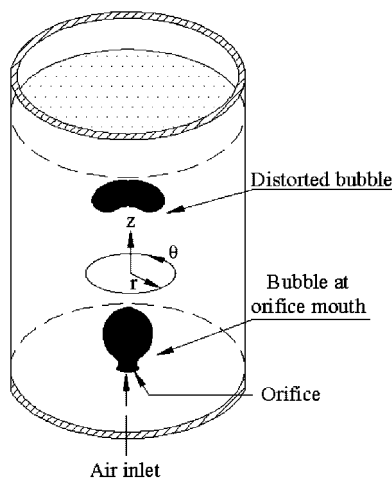

Figure 3. Schematic diagram of case study 1.

assumes the interface to be sharp and abrupt which eventually restricted the authors to accurately study the rise of gas bubble after detachment from the orifice mouth. In the present study DI concept has been incorporated in SPH to equip the methodology for complex simulation of formation of bubbles and their subsequent rise in a liquid column. Air is injected from a constant pressure chamber below the orifice. Air chamber is maintained at a constant pressure corresponding the required velocity head through the orifice. For first few bubbles it is assumed that constant velocity through the orifice is equivalent to the constant pressure condition in the air tank.

Figure 3 schematically represents the formation of a gas bubble at a submerged orifice. After the growth of the bubble it departs the orifice and rises through the liquid pool as depicted in the figure.

The process of evolution and free rise of bubble has been simulated by both the methodologies of DI-SPH and the basic SPH. To make a comparison we have considered the work of Buwa *et al.* [71] and simulated the process for identical conditions. Buwa *et al.* [71] have used combined
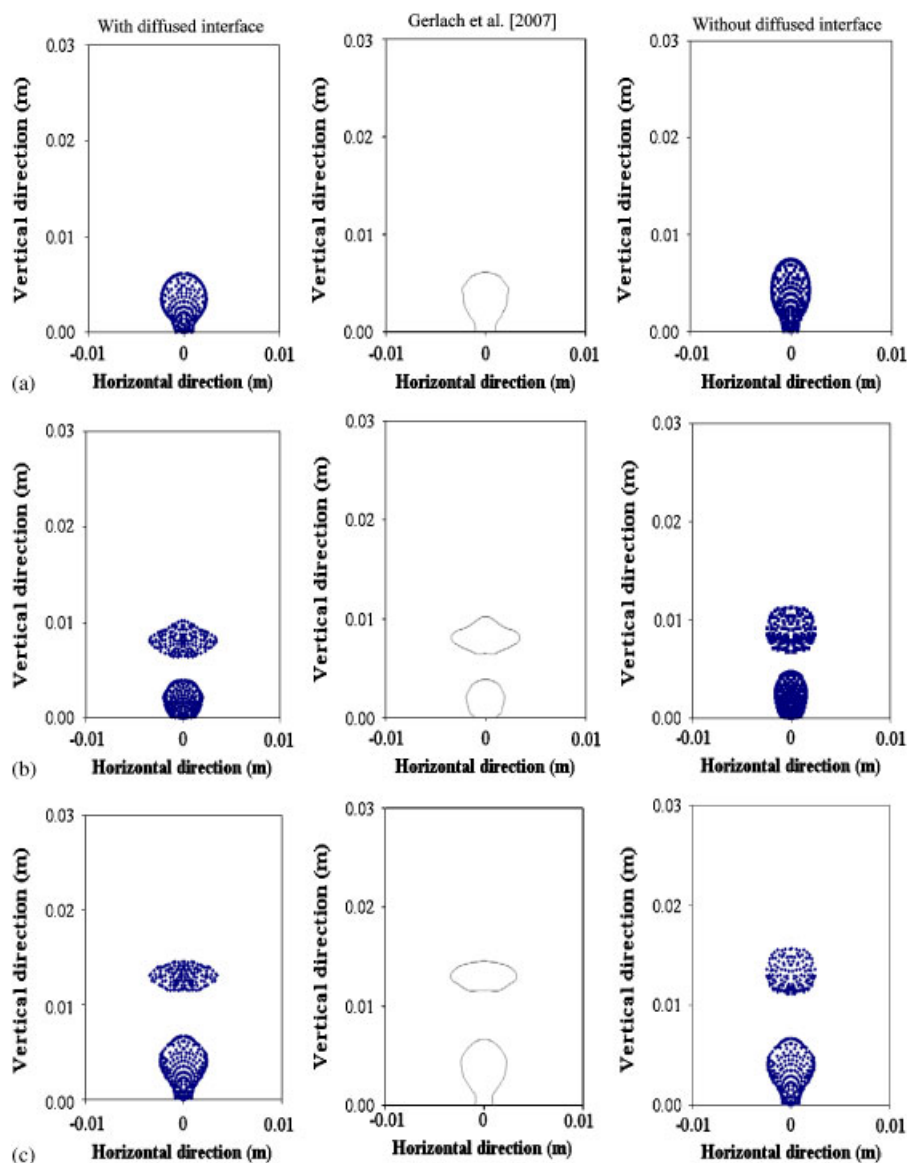

Figure 4. Bubble evolution and its free rise in liquid column with and with out DI method: (a) 0.018 s; (b) 0.041 s; (c) 0.0645 s; (d) 0.0875 s; and (e) 0.11 s.
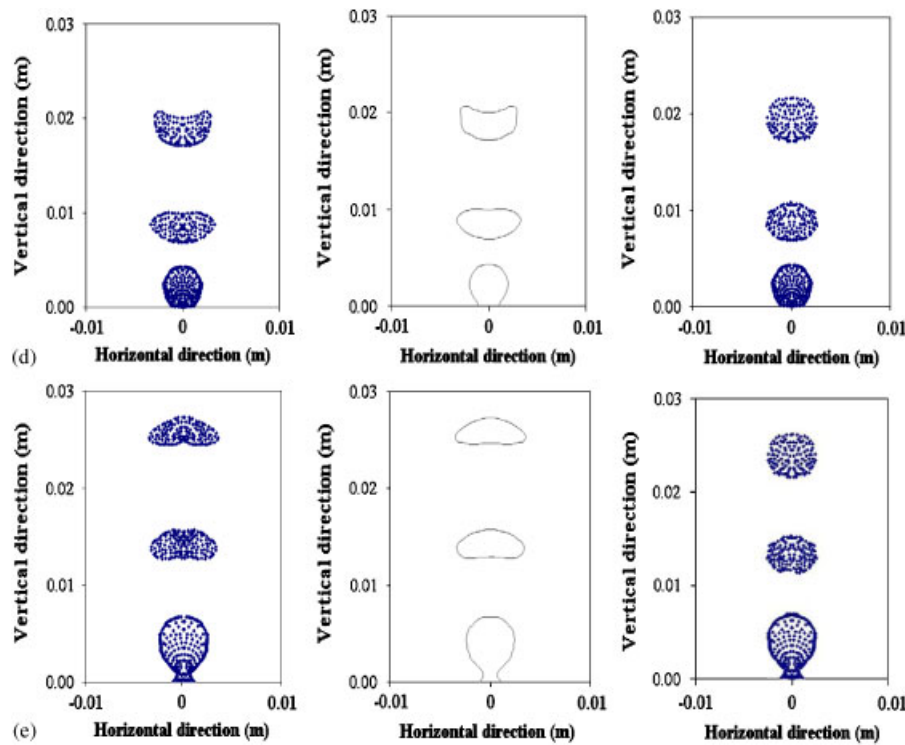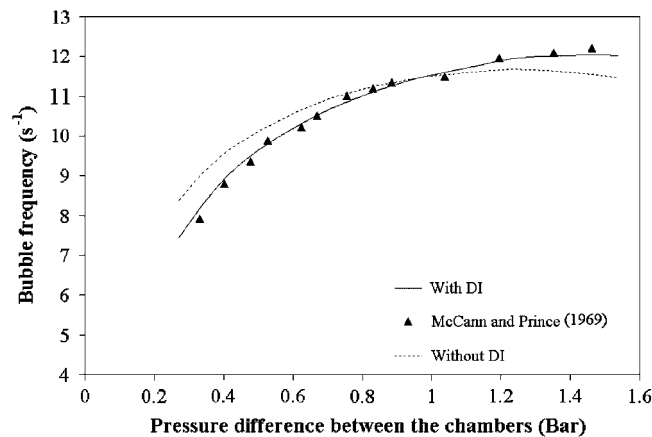
Figure 4. *Continued.*

Figure 5. Prediction of bubble frequency for different chamber pressure by DI-SPH and basic SPH.

LS and VOF method for capturing the interface. Air and water (surface tension $0.072\,\mathrm{N/m}$) has been used as the gaseous and liquid phases, respectively. Volume flow rate through the orifice of $2\,\mathrm{mm}$ diameter is kept at $100\,\mathrm{cm}^3/\mathrm{min}$.

A cylindrical control volume was taken as the physical domain for computation. Both the diameter and the height of the domain were taken as $300\,\mathrm{mm}$. It was equally divided by a solid plate of zero thickness into the liquid (upper) and air (lower) regions. The orifice hole is situated at the centre of the solid plate. Following a cylindrical Cartesian coordinate system (Figure 3), initially the particles are placed on a number of horizontal planes with uniform spacing Δz. In a horizontal plane, particles are positioned in a number of circular arrays placed at an equal radial spacing Δr. Again, in a particular circular array the particles are uniformly spaced with a circumferential
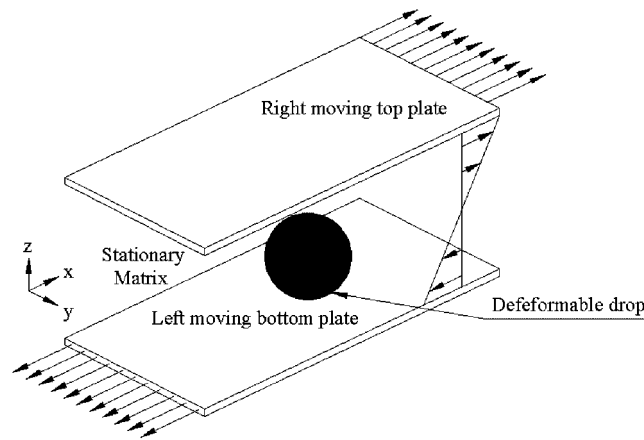
Figure 6. Schematic diagram of case study 2.

spacing Δs. To start with we have taken $\Delta z = \Delta r = \Delta s$. Based on a rigorous study the optimum value of particle spacing was determined as 0.1 mm. Surface area of the interface and the centre of gravity of the bubble evaluated from the data of reported literature are considered to be the defining parameter for the optimization. Optimum spacing has been fixed whenever the error in prediction of both surface area and centre of gravity reaches within $\pm$ 1%. Time step is taken as 5×10^{-4} s after a study for time resolution.

In Figure 4 bubble evolution for a duration of 70–162 ms has been depicted as obtained from our simulations *vis-à-vis* the simulation results of Buwa *et al.* [71]. At a first glance the striking trend matching between the figures depicted in the different columns of the figures is obvious. However, a critical inspection helps to bring out the differences. Both SPH and DI-SPH simulations generate almost similar shape of the gas bubble as long as it is attached to the orifice, although the former simulation shows a tendency for the bubble to get an elongated shape. It can be seen that SPH methodology can efficiently model the bubble evolution at submerged orifice but bubble dynamics after the detachment from the orifice mouth is not tracked well by this technique. On the other hand, DI-SPH methodology tracked both the evolution of bubble as well as its rise through liquid column with a good accuracy in comparison to the results shown by Buwa *et al.* [71]. It needs to be mentioned further that the results of Buwa *et al.* [71] replicate the experimental results of Zhang and Shoji [73] and depicts an excellent agreement. In that regard the present DI-SPH solution also matches with the same experimental results very closely.

As the bubble is attached at the orifice mouth, the force due to gas pressure is most dominant for the shape evolution. Basic SPH methodology tracks this force effectively which can be seen from the good agreement of the bubble at the orifice mouth. But after detachment from the orifice mouth bubbles no longer remain spherical due to the effect of buoyancy and surface tension forces. Inherent deficiency of the sharp interface technique in modelling the interfacial tension may be the possible reason for the mismatch in bubble shape after it is detached. Once DI is incorporated in SPH, the algorithm enables the simulation of both free rising bubbles and the bubbles pinned at the orifice mouth with adequate accuracy. After the detachment the bubbles become oblate which is tracked well by DI-SPH but is not captured by basic methodology. Even change of bubble shape during its rise through the liquid column is well tracked by DI-SPH that can be observed from the results shown in the first column of Figure 4.

In Figure 5 bubble frequency calculated using SPH methodology is compared with the experimental data of McCann and Prince [74]. Additionally, the simulation by DI-SPH for the same parametric combinations has also been superimposed in the same figure. The simulation through DI-SPH shows a better agreement with the experimental data and establishes the improvement due to the incorporation of DI.
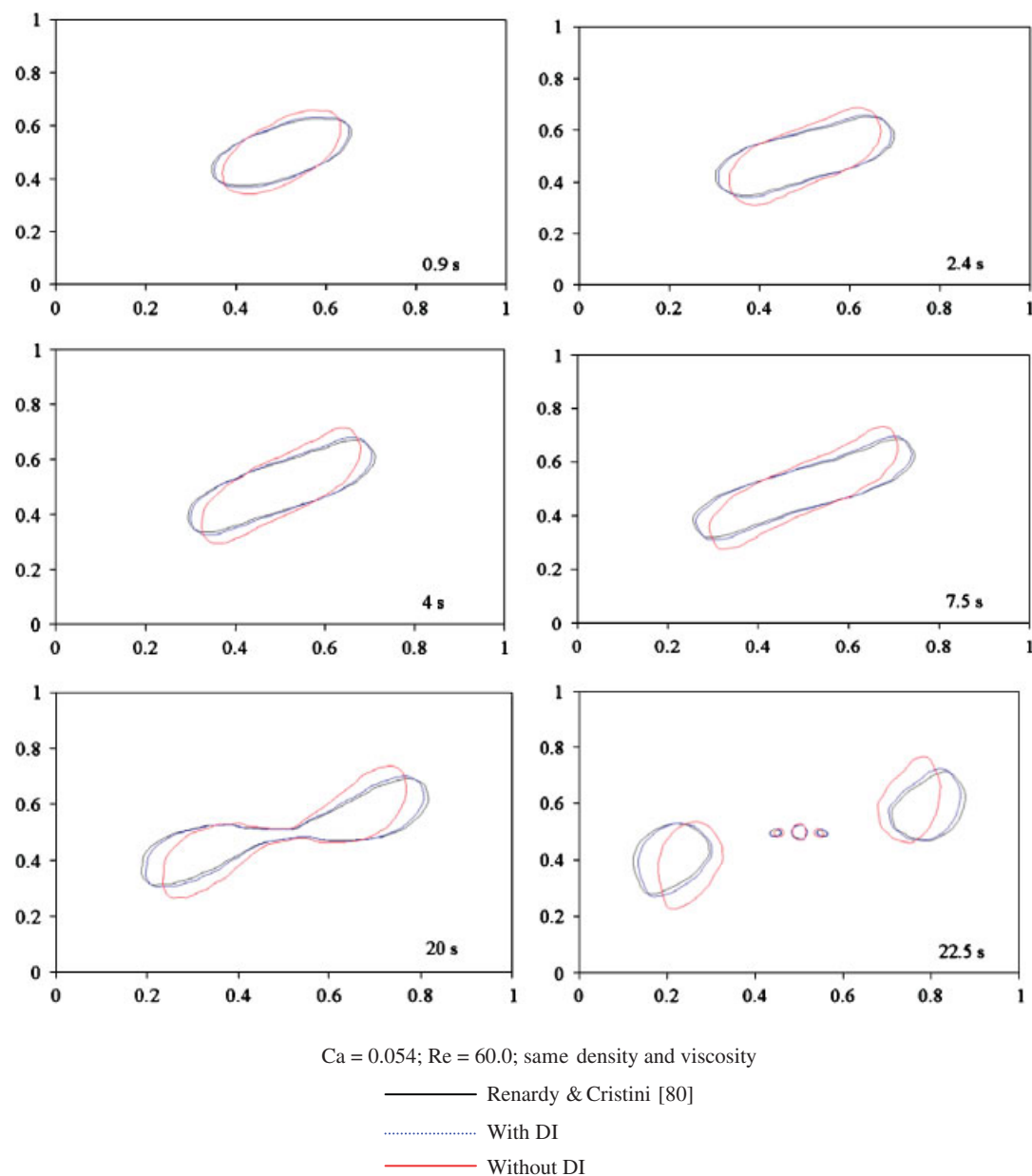
Ca = 0.054; Re = 60.0; same density and viscosity

———— Renardy & Cristini [80]

·············· With DI

———— Without DI

Figure 7. Transient drop deformation and break up due to shear flow by
DI-SPH and basic SPH methodology.

3.2. Drop in a shear flow

Deformation of a drop and its breakup into finer droplets are commonly encountered in various
systems including microfluidic devices and emulsification processes. The phenomenon is of funda-
mental importance in dispersion science and shows a great potential in micro mixing and micro
reaction. To manipulate a drop in an immiscible matrix confined in a conduit, application of
shear flow in the matrix is a common trend. Starting from initial work of Taylor [75] several
authors [76–78] have attempted to analyse this problem in order to understand the complex inter-
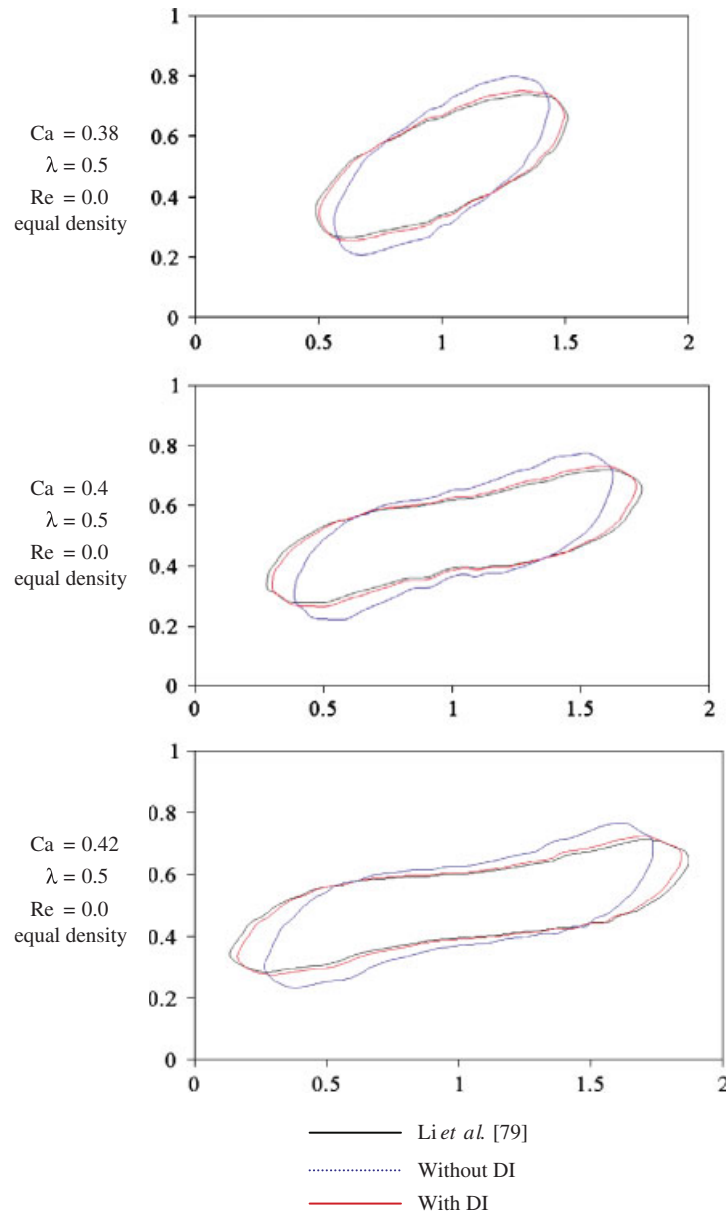play between inertia, viscous and surface tension forces. The important non-dimensional numbers

Figure 8. Prediction of drop deformation for various *Ca* number using DI-SPH method.

governing the phenomena are Capillary number (Ca), Reynolds number (Re), and viscosity ratio (λ); and are defined as:

$$Ca = \frac{\mu_m \beta a}{\sigma_{md}}, \quad Re = \frac{\rho_m \beta a^2}{\mu_m} \quad \text{and} \quad \lambda = \frac{\mu_d}{\mu_m} \tag{26}$$

Here, β is the shear rate and m and d stands for matrix and droplet. a is the initial droplet radius.

Li *et al.* [79] proposed a critical Ca over which the drop deforms into a dumbbell shape and daughter drops generate due to end pinching. Renardy and Cristini [80] examined different stages of drop break up through VOF-based numerical simulation. As drop deformation in shear flow is governed by various body and surface forces, complex interfacial configurations are obvious. It is expected that the use of particle-based methodology like SPH can successfully model the
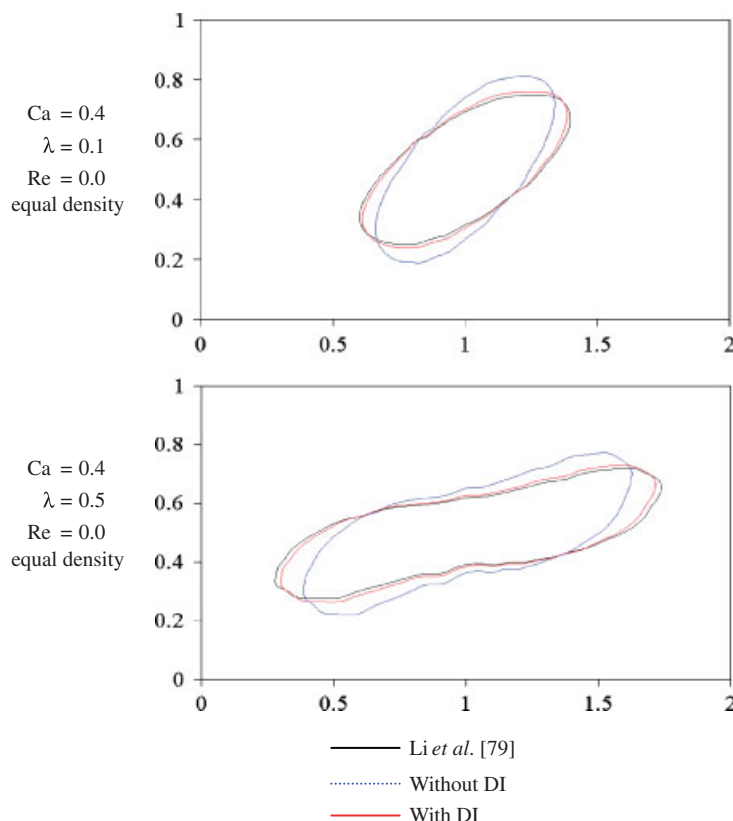
Figure 9. Prediction of drop deformation for various viscosity ratio between drop and matrix using DI-SPH method.

phenomena due to the inherent flexibility of the method in tracking dynamic interfaces. But during shearing of liquid drop, interfacial forces becomes dominant which need a robust treatment of sudden property jump across the interface. Proposed DI-based SPH model is employed to investigate the drop deformation in shear flow. To demonstrate the advantages of DI-SPH model over basic SPH methodology results have also been obtained by basic SPH simulation.

The schematic representation of the problem considered is shown in Figure 6. Initially a spherical fluid drop in the matrix of another immiscible fluid is confined between two rectangular parallel plates. Due to the motions of the plates in reverse direction the centrally placed drop is subjected to a shear field. Drop deformation and break up in a shear flow is simulated using 3D DI-SPH algorithm for $Ca = 0.054$ and $Re = 60$. Particles are initially placed uniformly in the domain with 0.001 mm initial spacing after a systematic study for the optimum spacing. Simulation is forward marched with a step of 10^{-3} s to avoid any numerical instability. The motion of the matrix fluid through the finite length of the channel has been modelled using periodic boundary conditions at the channel ends. Viscosity and density of the drop and matrix are assumed the same for the simulation. The same problem has also been solved numerically using basic 3D SPH model. Results obtained from both the schemes are compared with the numerical data of Renardy and Cristini [80] in Figure 7. It may be noted that Renardy and Cristini [80] used VOF to solve this problem. All the simulations indicate that the spherical droplet takes up an ellipsoidal shape to start with. The major axis of the ellipsoid makes an angle with the channel axis such that the leading edge points the positive x direction. The ellipsoid elongates further to form a two lobed drop with a narrow connecting finger. The two lobes finally break into two small drops and the connecting finger fragments into a number of tiny droplets. It can be observed that the numerical simulations through DI-SPH and the VOF-based model of Renardy and Cristini [80] produce excellent matching as far as drop shapes are concerned. The simulation through SPH with sharp interface gives noticeable deviations in the
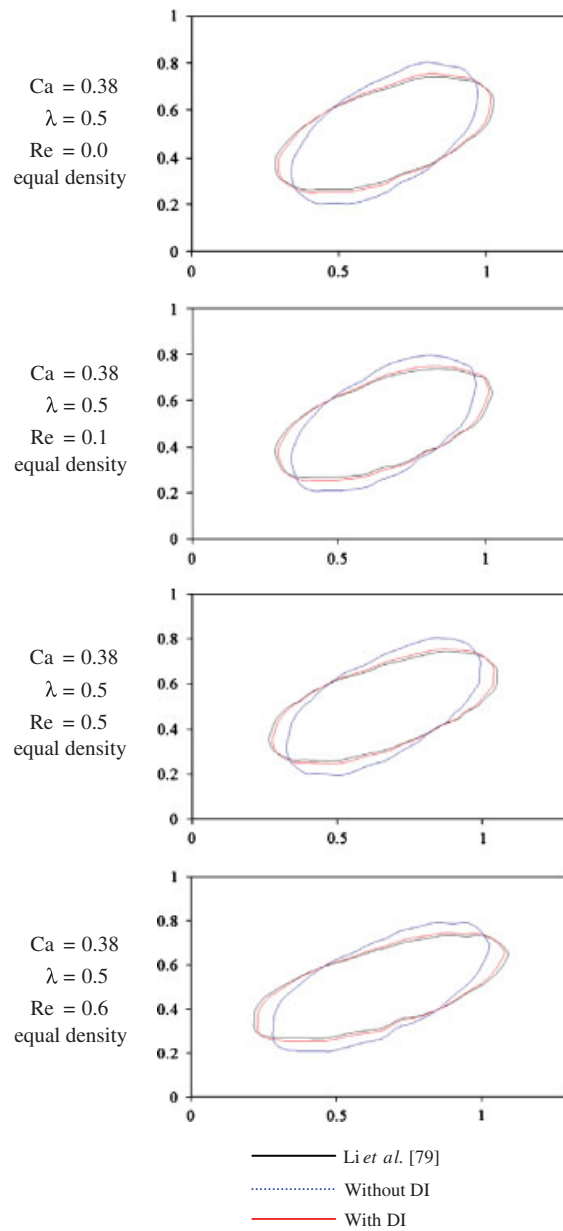
Figure 10. Prediction of drop deformation for various *Re* number using DI-SPH method.

shape at every stages of drop evolution. The improvement due to the incorporation of DI in the basic SPH model is clear from this comparison. Basic SPH model efficiently captures the shearing of liquid drop but its interaction with the continuum is not well tracked when a sharp interface is taken. As a result the angle generated between the daughter bubbles are also not tracked well in basic SPH methodology. Incorporation of DI in SPH improves the prediction in all respect.

To test the suitability of the developed methodology over a range of fluid properties simulations have next been done varying the non-dimensional numbers. To examine the effect of surface tension drop shapes have been evaluated for different *Ca*. A high value of viscosity has been taken for the matrix fluid to avoid any breakage. This renders the Reynolds' number close to zero. Drop viscosity is taken as half of the matrix viscosity. Equal densities have been taken for both the fluids. Drop motion and deformation have been simulated using SPH and DI-SPH for three different *Ca* (0.38, 0.4 and 0.42). It has been observed that drop becomes elongated in the reported ranges of
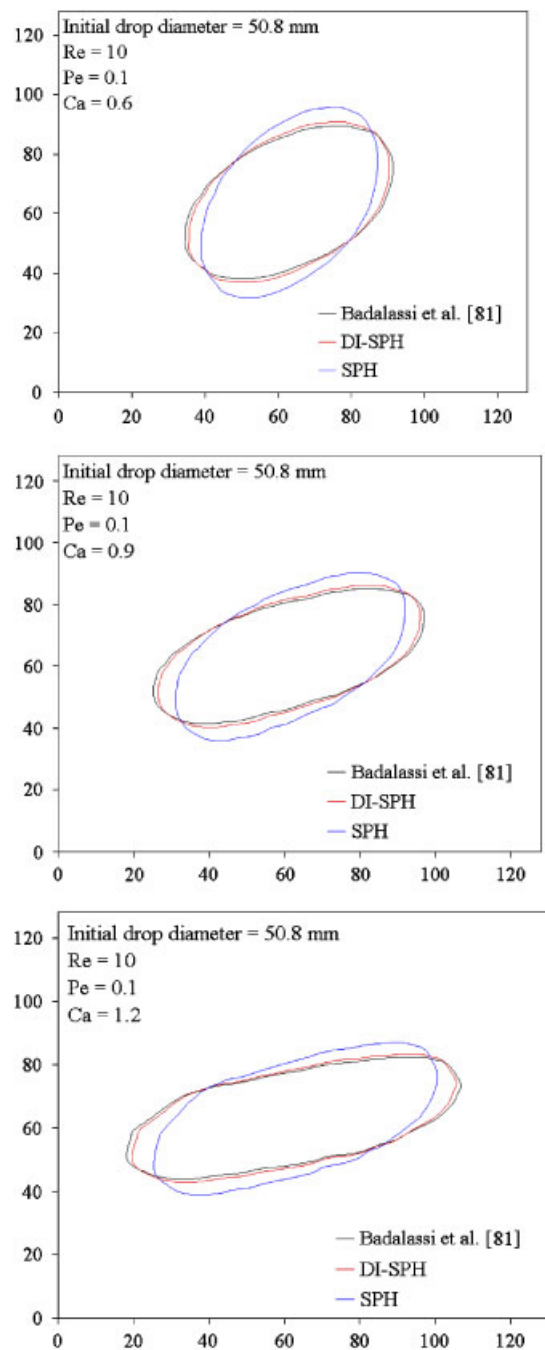
Figure 11. Validation of DI-SPH methodology with numerical results of Badalassi *et al.* [81].

Ca value and reaches at a stable shape from which further elongation is not observed. Figure 8 shows the above simulation along with the results reported by Li *et al.* [79]. In this case also the DI-SPH simulation gives a closer agreement with the results of Li *et al.* [79]. For high *Ca* value drop elongation ultimately tends towards the pinch off.

Effect of the variation in drop viscosity is reported in Figure 9. Viscosity of the drop is lowered in comparison to the viscosity of the matrix assuming very low density of both the fluids such that the *Re* is close to zero. In Figure 9 simulated results for viscosity ratios of 0.1 and 0.5 and *Ca* = 0.4 are shown for the stable drop shape. As the viscosity ratio increases the drop becomes
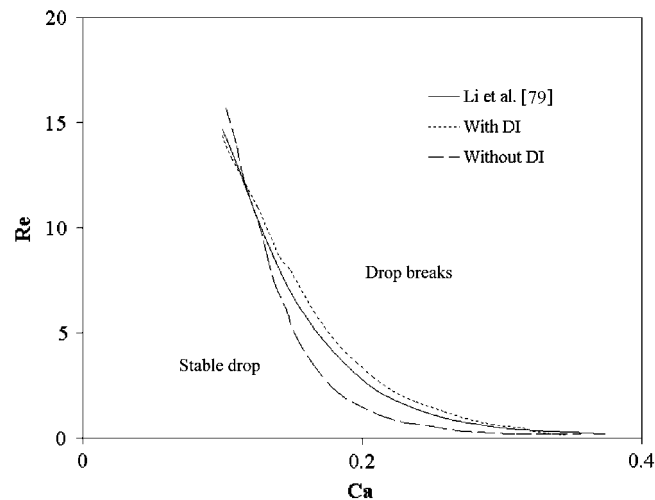
Figure 12. Estimation of transition line for deformed drop and its break up for various *Ca* and *Re* number using SPH-DI method.
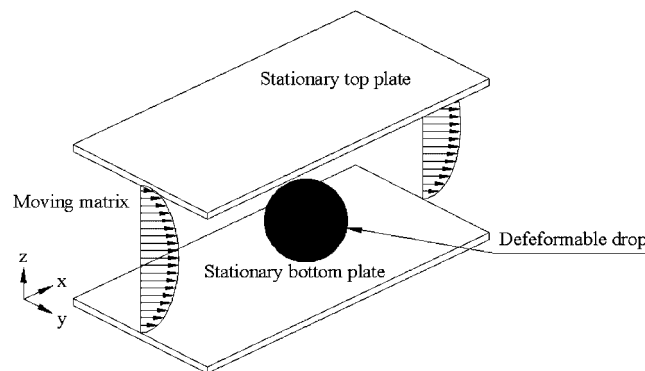

Figure 13. Schematic diagram of case study 3.

more slender and filamental. Nevertheless, like all the previous cases DI-SPH results agree very well with the VOF-based simulation of Li *et al.* [79].

Similarly, the effect of *Re* on stable drop shape is shown in Figure 10 for fixed values of λ and *Ca* and equal densities of the fluids. Increase in *Re* enhances the shearing action and elongates the drop as expected. The improvement in the prediction of the drop shape through the incorporation of DI is also obvious from this exercise.

Finally, numerical results of the present methodology have been compared with the reported numerical simulation of Badalassi *et al.* [81]. Badalassi *et al.* [81] used coupled Cahn–Hilliard/Navier–Stokes system for modelling of drop deformation under shear flow. Simulations have been made using the developed DI-SPH methodology for three different *Ca* number (0.6, 0.9 and 1.2) keeping the *Re* (0.1) fixed. Badalassi *et al.* [81] used DI concept and defined Peclet number based on the interface thickness and liquid mobility (3×10^{-6}). Same has been used for the present simulations. Figure 11 shows the comparisons of drop shapes reported by Badalassi *et al.* [81] and those obtained through numerical simulations using DI-SPH and SPH. It is clear from the figure that prediction of DI-SPH methodology is matching well with Badalassi *et al.* [81] compared to basic SPH methodology. The above comparison once again establishes the improvement in the prediction of SPH method by the incorporation of DI. From the above discussion it is seen that the drop elongates with the increase of both *Ca* and *Re*. Depending on the values of these two numbers one may get an elongated drop shape which does not change further
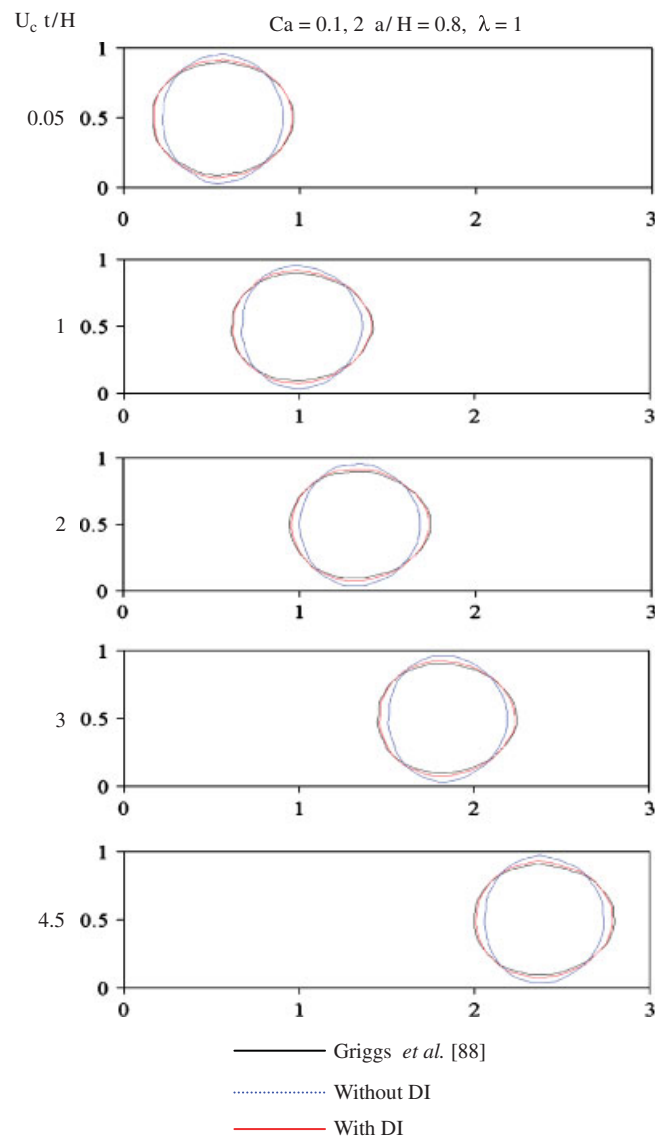
Figure 14. Deformable drop under parabolic flow ($Ca=0.1$): prediction of DI-SPH, basic SPH and Griggs *et al.* [88].

and a drop breakup is not encountered. Alternately the elongation may continue and ultimately results in break up of the drop. For a given *Ca* one can identify a critical *Re* above which drop break up occurs. Li *et al.* [79] have constructed a transition curve for drop break up in *Ca–Re* plane. The same exercise has been repeated using SPH simulation adopting both sharp and DI and the results are shown in Figure 12. The DI-SPH prediction follows the curve by Li *et al.* [79] closely while the prediction through basic SPH deviates from both these curves over a range of *Ca*. All the exercises in this section demonstrate that SPH can simulate the deformation of immiscible drops in shear flow successfully. However, incorporation of DI in the basic algorithm of SPH provides finite improvement in prediction.

3.3. Drop deformation in pressure driven flow

Immiscible drops undergo deformation not only in a shear flow but also during their motion in pressure driven flow through a closed conduit. Such drop deformation is important in different chemical processes and microfluidic systems. Transport and deformation of cells through biofluidic
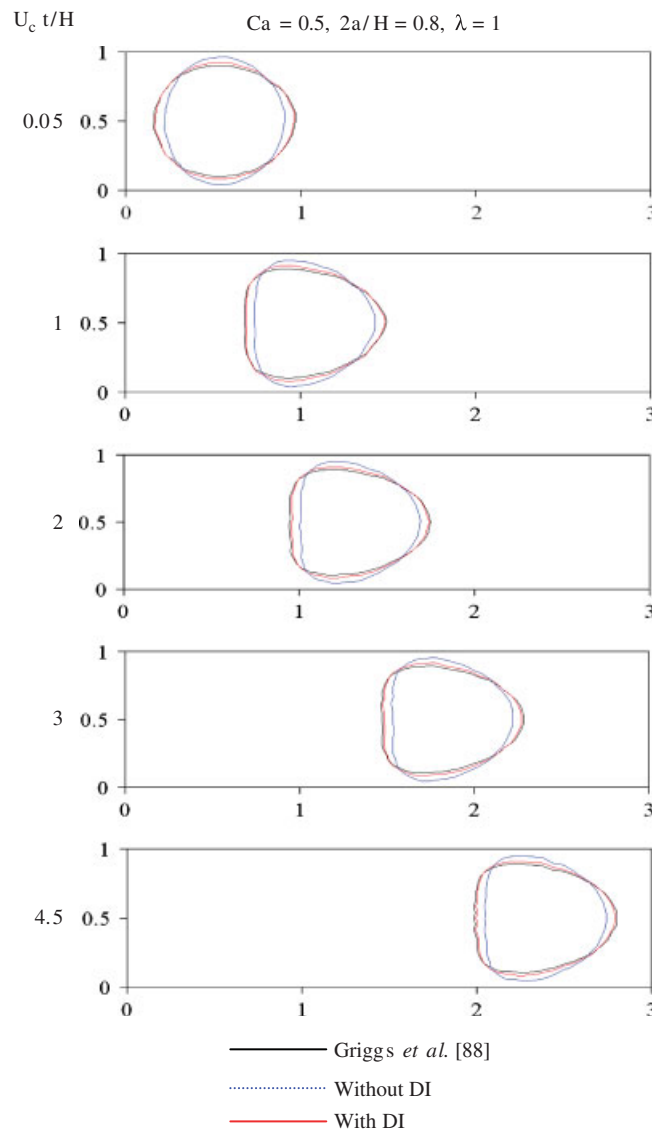
$U_c\,t/H$ $Ca = 0.5,\ 2a/H = 0.8,\ \lambda = 1$

Figure 15. Deformable drop under parabolic flow ($Ca = 0.5$): prediction of DI-SPH, basic SPH and Griggs *et al.* [88].

capillaries requires a thorough analysis. In spite of some commonality between the drop deformation in shear flow and pressure driven flow there are some important differences. After the application of shear a drop tends to align itself at an angle with the channel axis. On the contrary, the axis of symmetry of a drop is parallel to (or coincides with) the channel axis in pressure driven flow. As a result the tail end of the bubble near the channel axis gets elongated and in extreme case have a tendency to tear off from the parent drop. This is different from the deformation a drop experiences in a shear flow and needs a separate study.

To examine the utility of the DI scheme in SPH methodology further we have studied a deformable drop under the influence of parabolic flow inside parallel channels. The phenomenon is schematically depicted in Figure 13. Hiller and Kowalewski [82] first experimentally observed a dilute suspension of liquid drop in plane poiseuille flow. Shapira and Haber [83] used method of reflection to obtain analytical drop shape under the influence of drag force and pressure field. Couillette and Pozrikidis [84] studied pressure driven motion of a deformable drop through a cylindrical tube. A good review on the motion of large drops due to parabolic flow through a
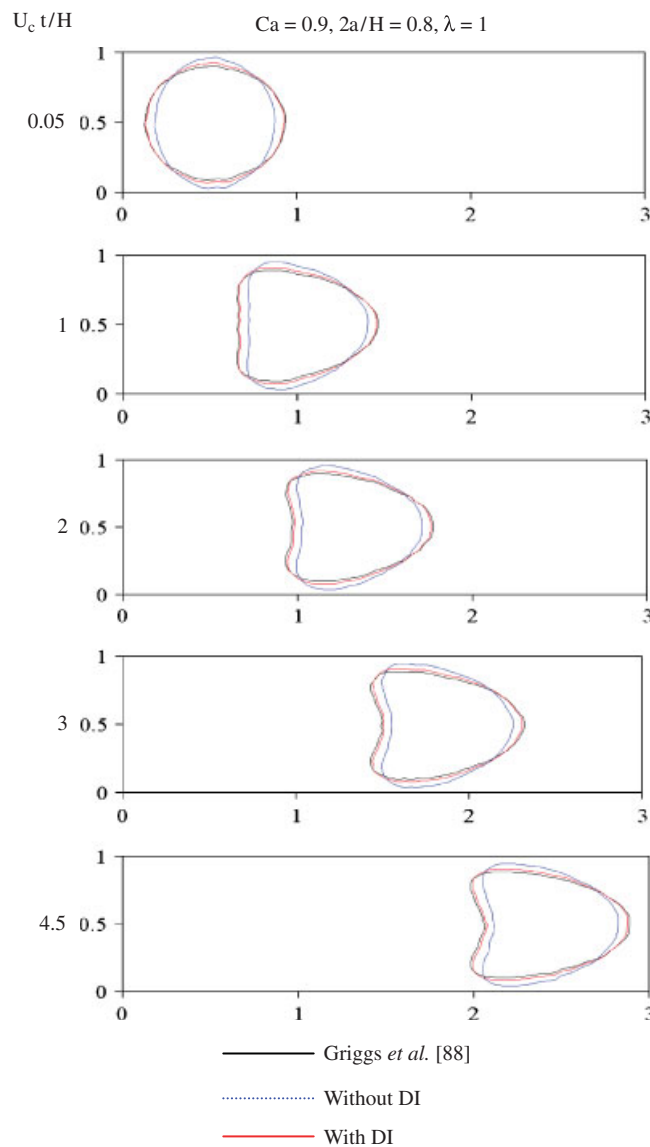
Figure 16. Deformable drop under parabolic flow ($Ca = 0.9$): prediction of DI-SPH, basic SPH and Griggs *et al.* [88].

circular tube can be found in Olbricht [85]. Mortazavi and Tryggvason [86] used front tracking algorithm for numerical simulation of drop deformation due to parabolic flow and showed the dependence of drop deformation over viscosity ratio and *Re* number. Keh and Chen [87] used a combined analytical–numerical approach to study the deformation of a droplet between two parallel plane walls and reported that minimum drag force can be felt by a drop when it is placed at the midplane of the parallel plates. Recently, Griggs *et al.* [88] solved a three-dimensional motion of a drop inside two parallel plates experiencing low *Re* number poiseuille flow using boundary integral method (BIM). They showed that the drop deformation is increased as the *Ca* number increases.

Present DI-SPH methodology has been used for the simulation of drop deformation under parabolic flow situation. Simulations have also been done by the basic SPH methodology for a comparison. Particle spacing and time step are kept identical as maintained in the previous case. For
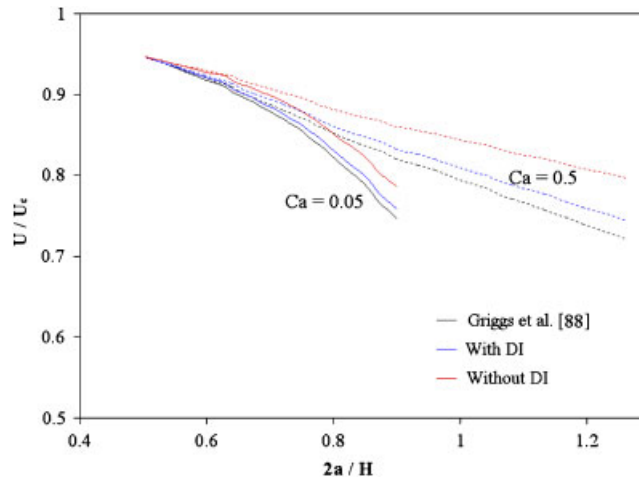
Figure 17. Estimation of drop velocity using DI-SPH and basic SPH for different sized drop and different *Ca* number under the influence of parabolic flow.

the parabolic flow, fluid properties can be expressed in terms of velocity in the channel midplane (U_c) and Capillary number (*Ca*). *Ca* is defined as:

$$Ca = \frac{\mu_m U_c}{\sigma} \qquad (27)$$

Initial drop size is also an important parameter for such type of flow. In all the simulations initial drop radius is expressed in terms of the half channel width. In Figures 14–16 numerical simulation of DI-SPH methodology for drop deformation at different *Ca* number is shown along with the simulations of basic SPH methodology. It may be observed that drop deformation increases as *Ca* increases from 0.1 to 0.9. The droplet shapes predicted by the two variations of SPH have been compared with the numerical simulations of Griggs *et al.* [88]. The shapes obtained by these three different techniques are superimposed in the figure for a close comparison. In Figures 14–16 drop diameter is kept at 0.8 times of the channel width. In Figure 14 drop shape at different time level is shown for *Ca* value 0.1. It is clear that prediction of DI-SPH matches closely with the results of Griggs *et al.* [88] in comparison with basic SPH predictions. Similarly for more deformable drops (Figures 14 and 15) at higher *Ca* number DI-SPH gives better prediction compared to the basic SPH methodology. In all these results the limitation of the basic SPH simulation in capturing the nature and magnitude of drop elongation is obvious.

Drop velocity for various drop size is also computed using the DI-SPH methodology. Like the shape of the drop its velocity (*U*) is also influenced by a number of parameters. As the isolated drops tend to align them along the axis of the channel, a small drop will get transported through the central region of the channel and will not be affected much by the viscous effect due to their distance from the channel wall. The velocity of small drops is comparable to the centreline velocity of the parabolic velocity profile. The drop velocity also uniquely depends on the *Ca*. A large *Ca* signifies a greater deformation of the drop. As deformation elongates a drop its distance with the wall increases. Consequently the drop will move with a larger velocity. Further, the velocity varies with the drop size linearly for a large *Ca*. From Figure 17 it can be seen that all these features can be captured successfully [88] by the simulations based on SPH. However, incorporation of DI in SPH improves the simulation significantly over the entire range of drop diameter and for all the values of *Ca*. For the point of maximum deviation incorporation of DI in SPH improves the prediction from 85 to 95% for $Ca=0.5$ and from 92 to 95% for $Ca=0.05$.

It is interesting to study the deformation of drops whose size is larger compared with the channel width. Such drops can be conceived as ellipsoidal drop with its major axis aligned along the channel axis. For simulation we have considered a drop with 1.47*D* as major and 0.86*D* as minor diameter and with a *Ca* of 0.5. As such a drop fits very closely inside the channel, viscosity effects will
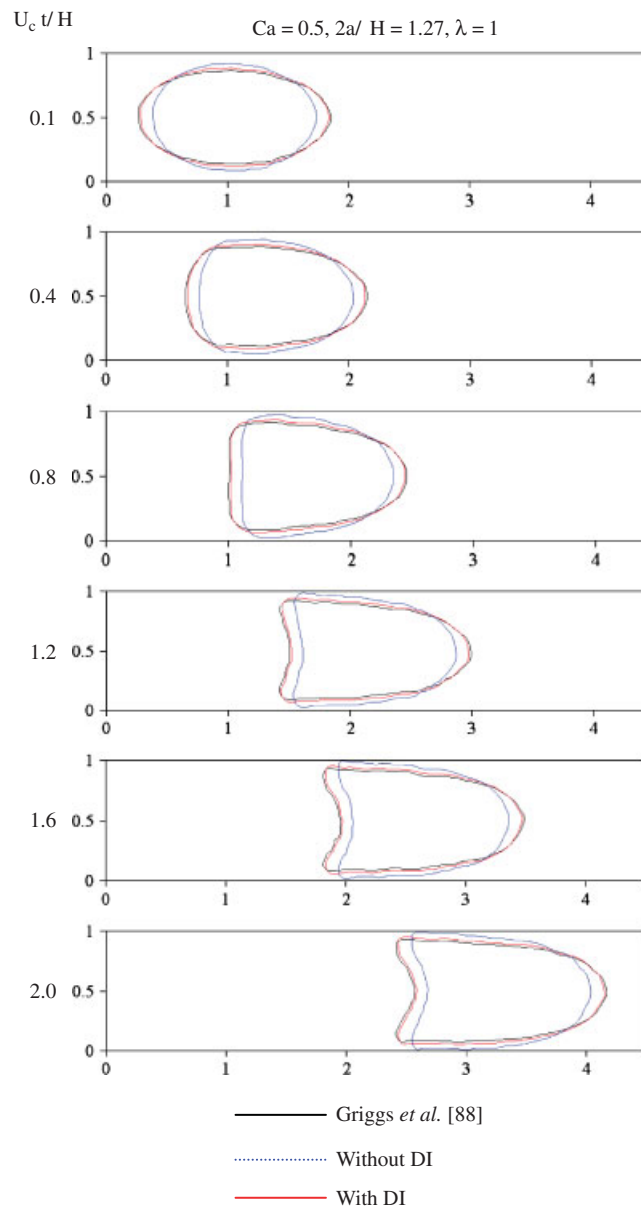
Figure 18. Large deformable drop ($2a/H = 1.27$) under parabolic flow ($Ca = 0.5$): prediction of DI-SPH, basic SPH and Griggs *et al.* [88].

dominate. Simulation of deformation of such droplets becomes challenging [88]. A large droplet closely fitting in a channel undergoes a thorough deformation during its motion. The leading front of the drop becomes pointed while the trailing edge flattens. Gradually a concavity develops at the trailing end of the drop and finally the droplet reaches a stable shape. Figure 18 depicts the development of the drop shape simulated by SPH and DI-SPH formulations. The agreement between the results of DI-SPH simulation and boundary integral computation is superior as has been observed in the earlier cases.

Griggs *et al.* [88] studied the effect of viscosity ratio (λ) on the propagation of large drops through channels. Such drops initially undergo a deformation as described above. During this period its velocity decreases continuously. Once it reaches a stable shape it also attains a steady velocity. The behaviour is depicted in Figure 19. The time taken to attain the stable shape increases with the drop viscosity with an associated decrease in its steady velocity. The results obtained by
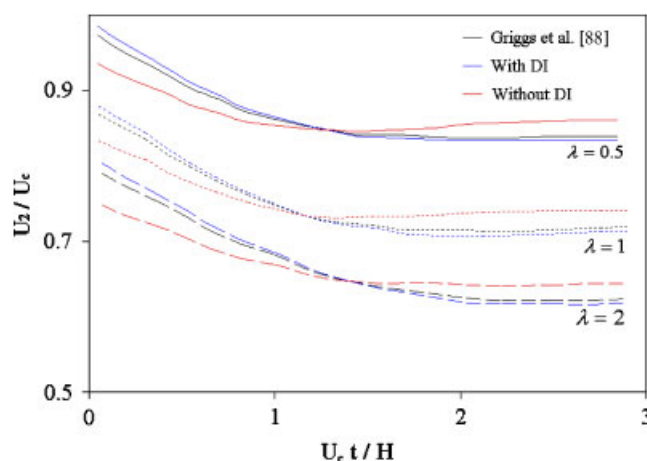
Figure 19. Estimation of transient drop velocity for different drop viscosity using DI-SPH methodology and basic SPH methodology.

DI-SPH methodology show substantial improvement [88]. The maximum error of the prediction reduces from 3 to 0.5%.

4. CONCLUSION

The concept of DI has been incorporated in the Lagrangian-based CFD simulation of SPH. A smooth variation of chemical potential between two bulk phases have been considered using Cahn–Hilliard equation as has been done by other researchers [39] for the incorporation of DI in different grid-based computational techniques. It may be noted that rarely any effort has been made to combine the concept of DI with SPH. To the best of the knowledge of the authors, no other research groups have yet tried to couple DI based on the variation of chemical potential along with SPH. Present model proposes particle-based transport equation for the order parameter which is a definite improvement over the DI-SPH model suggested by Xu *et al.* [46].

The momentum equation has been suitably modified to adopt the continuous field of chemical potential in SPH. Fluid properties in SPH are estimated considering the influence of the neighbouring particles through the use of a suitable smoothing length. The same concept has been extended to determine the chemical potential of a particle-based system on the colour code of its surrounding neighbours. In the next step, the Cahn–Hilliard equation along with suitable boundary conditions has been used to refine the value of chemical potential. In the absence of phase change or mass diffusion the boundary conditions include no flux across the interface and local equilibrium at the triple line. Finally the momentum equation near the interface needs a modification so that the interparticular interactions due to the interface curvature can be accounted for.

The proposed methodology has been put to rigorous tests considering a number of two phase problems. Three different case studies namely (i) evolution and free rise of a bubble from a submerged orifice, (ii) drop deformation and break up in shear flow and (iii) movement of a deformable drop in pressure driven flow using SPH both with sharp interface and DI schemes have been simulated. Predictions have been compared with the results already published in the literature. In all the cases DI-SPH simulation provides discernable improvement over the SPH simulation with sharp interface.

To test the viability of the DI-SPH scheme three different case studies have been modelled. Mostly the comparison has been done with the computational results of the other researchers. These results have been picked up so that the DI-SPH scheme can be calibrated with different accepted techniques of interface simulations, such as CSF-based VOF [80], combined LS and VOF [70] and BIM [88]. Moreover, one set of results from the present simulation (Figure 11) compares very well with a grid-based DI computation of Badalassi *et al.* [81].

It also needs to be mentioned that the results of the present simulation for drop evolution at submerged orifice compares favourably with the experimental observation of Zhang and Shoji [73] and matches very well with the bubble frequency data of McCann and Prince [74]. This enhances the confidence regarding the accuracy of the present methodology. Finally, it may be commented that it is possible to use the idea of DI also in Lagrangian formulation of fluid dynamics and the present scheme based on this idea is suitable for a variety of problems with complex interfacial configurations.

NOMENCLATURE

a	drop diameter (m)
B	empirical constant in Equation (9) ($\mathrm{Nm^{-2}}$)
c_i	velocity of sound through the medium ($\mathrm{ms^{-1}}$)
Ca	drop capillary number derived in Equations (26) and (27) (dimensionless)
Cap	capillary number (dimensionless)
Cn	Cahn number (dimensionless)
C_s	colour attribute of the particle s (dimensionless)
D	empirical constant in Equation (10) (dimensionless)
f	empirical constant in Equation (9) (dimensionless)
$f(x)$	value of function at special coordinate x
f_{si}	surface tension force per unit volume ($\mathrm{kgm^{-2}s^{-2}}$)
$F(R)$	Lennard-Jones force at the boundary ($\mathrm{kgms^{-2}}$)
F_{si}	surface tension force ($\mathrm{kgm\,s^{-2}}$)
g	gravitational acceleration ($\mathrm{ms^{-2}}$)
h	smoothing length (m)
H	distance between parallel plates (m)
k	mobility of the particle ($\mathrm{m^2V^{-1}s^{-1}}$)
k_{w}	wetting coefficient (dimensionless)
L_c	length scale of the drop (m)
m_i	mass of particle i (kg)
n	order of derivatives (dimensionless)
n_s	normal vector of the interface (dimensionless)
N	total number of particles (dimensionless)
p_i	pressure ($\mathrm{kgm^{-1}s^{-2}}$)
r_{ij}	scalar distance between two particles (m)
r_0	minimum distance between boundary particle and fluid particle (m)
Re	Reynolds number (dimensionless)
t	time (s)
U_{c}	centre line velocity of the matrix ($\mathrm{ms^{-1}}$)
v_i	velocity of particle i ($\mathrm{ms^{-1}}$)
v_{ij}	relative velocity of particle i and j ($\mathrm{ms^{-1}}$)
$W(x, h)$	smoothing function at position x having smoothing length h (dimensionless)
x_i	position vector (m)
x_{ij}	relative position vector between particles i and j (m)

Greek alphabets

Θ	domain of interest ($\mathrm{m^3}$)
α_c	empirical constant in Equation (11) (dimensionless)
β	shear rate ($\mathrm{s^{-1}}$)
β_c	empirical constant in Equation (11) (dimensionless)
δ	Dirac delta function (dimensionless)
δ_s	Dirac delta function along the interface (dimensionless)

η empirical constant in Equation (7) (m^2)
λ viscosity ratio (dimensionless)
μ_i viscosity of particle i $(kg\,m^{-1}\,s^{-1})$
ξ_i mean interfacial thickness (m)
π_{ij} Neumann–Richtmyer artificial viscosity $(kg\,m^{-1}\,s^{-1})$
ρ_0 density of the fluid at atmospheric temperature and pressure $(kg\,m^{-3})$
ρ_i density of particle i $(kg\,m^{-3})$
σ_{lg} surface tension of liquid and gas phase $(kg\,s^{-2})$
ϕ_i chemical potential of ith particle (Gibbs)
Δt time step (s)

REFERENCES

1. Panton RL. *Incompressible Flow*. Wiley: New York, 1984.
2. Young T. On the cohesion of fluids. *Philosophical Transactions* 1805; **95**:65–87.
3. Laplace PS. *Mécanique céleste*. Gauthier-Villars et fils: Paris, 1805.
4. Gauss CF. Principia Generalia Theoriae Figurae Fluidorum. *Werke* 1830; **5**:31.
5. Poisson SD. Nouvelle Théorie de l'action capillaire. *Annalen der Physik* 1832; **101**(6):270–287.
6. Maxwell JC. Capillary action. *Encyclopedia Britannica* (9th edn). Encyclopedia Britannica Inc.: New York, 1876.
7. Gibbs JW. On the equilibrium of heterogeneous substances. *Transactions of the Connecticut Academy* 1876; **3**:108–248.
8. Rayleigh L. On the theory of surface forces—II Compressible fluids. *Philosophical Magazine* 1892; **33**:209–220.
9. van der Waals JD. The thermodynamic theory of capillarity under the hypothesis of a continuous variation of density. *Verhandelingen der Koninklijke Nederlandsche Akademie van Wetenschappen te Amsterdam* 1893; **1**(8):21–65.
10. Korteweg DJ. Sur la forme que prennent les équations du mouvements des fluides si l'on tient compte des forces capillaries causées par des variations de densité considérables mais continues et sur la théorie de la capillarité dans l'hypothése d'une variation continue de la densité. *Archives Néerlandaises des Sciences Exactes et Naturelles Series II* 1901; **6**:1–24.
11. Lamb H. *Hydrodynamics*. Cambridge University Press: Cambridge, 1932.
12. Batchelor GK. *An Introduction to Fluid Dynamics*. Cambridge University Press: Cambridge, 1967.
13. Drazin PG. Reid WH. *Hydrodynamic Stability*. Cambridge University Press: Cambridge, 1981.
14. Noh WF, Woodward P. In *SLIC* (*Simple Line Interface Calculation*), van Dooren AI, Zandbergen PJ (eds). Lecture Notes in Physics, vol. 59. Springer: New York, 1976; 330–340.
15. Hirt CW, Nichols BD. Volume of fluid (VOF) methods for the dynamics of free boundaries. *Journal of Computational Physics* 1981; **39**:201–255.
16. Brackbill JU, Kothe DB, Ruppel HM. FLIP: a low-dissipation, particle-in-cell method for fluid flow. *Computer Physics Communications* 1988; **48**:25–38.
17. Sethian JA. *Level Set Methods*: *Evolving Interfaces in Geometry*, *Fluid Mechanics*, *Computer Vision*, *and Materials Science*. Cambridge University Press: Cambridge, 1996.
18. Tryggvason G, Unverdi SO. Computations of three-dimensional Rayleigh–Taylor instability. *Physics of Fluids A* 1990; **2**:656–659.
19. Morris JP. Simulating surface tension with smoothed particle hydrodynamics. *International Journal for Numerical Methods in Fluids* 2000; **33**:333–353.
20. Francois M, Shyy W. Computations of drop dynamics with the immersed boundary method, part 2: drop impact and heat transfer. *Numerical Heat Transfer Part B* 2003; **44**(2):119–143.
21. Popinet S. An accurate adaptive solver for surface-tension-driven interfacial flows. *Journal of Computational Physics* 2009; **228**:5838–5866.
22. Monaghan JJ. Simulating free surface flows with SPH. *Journal of Computational Physics* 1994; **110**:399–406.
23. Souto Iglesias A, Delorme L, Perez-Rojas L, Abril-Perez S. Liquid moment amplitude assessment in sloshing type problems with smooth particle hydrodynamics. *Ocean Engineering* 2006; **33**:1462–1484.
24. Lastiwka M, Basa M, Quinlan N. Application of 3D smoothed particle hydrodynamics to a shock tube flow: effect and control of particle distribution. *Proceedings of the 17th AIAA Computational Fluid Dynamics Conference*, Toronto, Canada, 6–9 June 2005.
25. Takeda H, Miyama SM, Sekiya M. Numerical simulation of viscous flow by smoothed particle hydrodynamics. *Progress of Theoretical Physics* 1994; **92**:939–960.
26. Libersky LD, Petscheck AG. Smoothed particle hydrodynamics with strength of materials. *Proceedings of the Next Free Lagrange Method Conference*, Jackson Hole, U.S.A., June 1990.
27. Hoover WG, Hoover CG. Smoothed-particle hydrodynamics and nonequilibrium molecular dynamics. *Annual Winter Meeting of the ASME*, New Orleans, LA, 1993.
28. Morris JP, Fox JP, Yi Z. Modeling low Reynolds number incompressible flows using SPH. *Journal of Computational Physics* 1997; **136**:214–226.

29. Colagrossi A, Landrini M. Numerical simulation of interfacial flows by smoothed particle hydrodynamics. *Journal of Computational Physics* 2003; **191**:448–475.
30. Tartakovsky A, Meakin P. Modeling of surface tension and contact angles with smoothed particle hydrodynamics. *Physical Review* 2005; **72**:026301.1–026301.9.
31. Chen JK, Beraun JE, Jih CJ. An improvement for tensile instability in smoothed particle hydrodynamics. *Computational Mechanics* 1999; **23**:279–287.
32. Hu XY, Adams NA. A constant-density approach for incompressible multi-phase SPH. *Journal of Computational Physics* 2009; **228**:2082–2091.
33. Grenier N, Antouno M, Colagrossi A, Le Touze D, Alessandrini B. An Hamiltonian interface formulation for multi-fluid free surface flows. *Journal of Computational Physics* 2009; **228**:8380–8393.
34. Liu GR, Liu MB. *Smoothed Particle Hydrodynamics—A Mesh Free Particle Method*. World Scientific: Toh Tuck Link, Singapore, 2003.
35. Anderson DM, McFadden GB, Wheeler AA. Diffuse-interface methods in fluid mechanics. *Annual Review of Fluid Mechanics* 1998; **30**:139–165.
36. Ding H, Spelt PDM. Inertial effects in droplet spreading: a comparison between diffuse-interface and level-set simulations. *Journal of Fluid Mechanics* 2007; **576**:287–296.
37. Cahn JW, Hilliard JE. Free energy of a non uniform system. I. Interfacial free energy. *Journal of Chemical Physics* 1958; **28**:258–267.
38. Antanovskii LK. A phase field model of capillarity. *Physics of Fluids* 1995; **7**:747–753.
39. Jacqmin D. Contact-line dynamics of a diffuse fluid interface. *Journal of Fluid Mechanics* 2000; **402**:57–88.
40. Liu C, Shen J. A phase field model for the mixture of two incompressible fluids and its approximation by a Fourier-spectral method. *Physica D* 2003; **179**:211–228.
41. Yue P, Feng JJ, Liu C, Shen J. A diffuse interface method for simulating two phase flows of complex fluids. *Journal of Fluid Mechanics* 2004; **515**:293–317.
42. Yue P, Zhou C, Feng JJ, Ollivier-Gooch CF, Hu HH. Phase-field simulations of interfacial dynamics in viscoelastic fluids using finite element with adaptive meshing. *Journal of Computational Physics* 2006; **219**:47–67.
43. Khatavkar VV, Anderson PD, Duineveld PC, Meijer HEH. Diffuse interface modelling of droplet impact. *Journal of Fluid Mechanics* 2007; **581**:97–127.
44. Tapia JJ, Lopez PG. Adaptive pseudospectral solution of a diffuse interface model. *Journal of Computational and Applied Mathematics* 2009; **224**:101–117.
45. van der Sman RGM, van der Graaf S. Emulsion droplet deformation and breakup with lattice Boltzmann model. *Computer Physics Communications* 2008; **178**:492–504.
46. Xu Z, Meakin P, Tartakovsky AM. Diffuse-interface modelling for smoothed particle hydrodynamics. *Physical Review E* 2009; **79**:036702.1–036702.7.
47. Gingold RA, Monaghan JJ. Smoothed particle hydrodynamics: theory and application to non-spherical stars. *Monthly Notices of the Royal Astronomical Society* 1977; **181**:375–389.
48. Randles PW, Libersky LD. Smoothed particle hydrodynamics: some recent improvements and applications. *Computer Methods in Applied Mechanics and Engineering* 1996; **139**:375–408.
49. Monaghan JJ. Smoothed particle hydrodynamics. *Reports on Progress in Physics* 2005; **68**:1703–1759.
50. Benz W. Smoothed particle hydrodynamics: a review. *NATO Workshop*, Les, Arcs, France, 1989.
51. Liu MB, Xie WP, Liu GR. Modeling incompressible flows using a finite particle method. *Applied Mathematical Modeling* 2005; **29**:1252–1270.
52. Liu MB, Liu GR, Lam KY. Investigations into water mitigations using a meshless particle method. *Shock Waves* 2002; **12**(3):181–195.
53. Das AK, Das PK. Bubble evolution through submerged orifice using smoothed particle hydrodynamics: basic formulation and model validation. *Chemical Engineering Science* 2009; **64**:2281–2290.
54. Van der Waals JD. The thermodynamic theory of capillarity under the hypothesis of a continuous variation of density. *Zeitschrift für Physikalische Chemie* 1894; **13**:657–725.
55. Cahn JW. On spinodal decomposition. *Acta Metallurgica* 1961; **9**:795–801.
56. Pismen LM. Diffuse-interface effects near a cusp singularity on a free surface. *Physical Review E* 2004; **70**:051604.1–051604.9.
57. Zhang Y, Wang H, Tang T. Simulating two phase viscoelastic flows using moving finite element methods. *Communications in Computational Physics* 2010; **7**(2):333–349.
58. Davidson L, Amick E. Formation of gas bubbles at horizontal orifices. *AIChE Journal* 1956; **2**(3):337–342.
59. Davidson JF, Schuler BOG. Bubble formation at an orifice in an inviscid fluid. *Transactions of the Institute of Chemical Engineers* 1960; **38**:144–154.
60. Khurana AK, Kumar R. Studies in bubble formation III. *Chemical Engineering Science* 1969; **24**:1711–1723.
61. Terasaka K, Tsuge H. Bubble formation under constant flow conditions. *Chemical Engineering Science* 1993; **48**(19):3417–3422.
62. Xie S, Tan RBH. Bubble formation at multiple orifices bubbling synchronicity and frequency. *Chemical Engineering Science* 2003; **58**(20):4639–4647.
63. Marmur A, Rubin E. A theoretical model for bubble formation at an orifice submerged in an inviscid liquid. *Chemical Engineering Science* 1976; **31**:453–463.
64. Tsuge H. Hibino SI. Bubble formation from an orifice submerged in liquids. *Chemical Engineering Communications* 1983; **22**:63–79.

65. Tan RBH, Harris IJ. A model for non-spherical bubble growth at a single orifice. *Chemical Engineering Science* 1986; **41**(12):3128–3182.
66. Kulkarni AA, Joshi JB. Bubble formation and bubble rise velocity in gas liquid systems: a review. *Industrial Engineering Chemical Research* 2005; **44**:5873–5931.
67. Oguz H, Prosperetti A. Dynamics of bubble growth and detachment from a needle. *Journal of Fluid Mechanics* 1993; **257**:111–145.
68. Wong H, Rumschitzki D, Maldarelli C. Theory and experiment on the low-Reynolds-number expansion and contraction of a bubble pinned at a submerged tube tip. *Journal of Fluid Mechanics* 1998; **356**:93–124.
69. Higuera F. Injection and coalescence of bubbles in a very viscous liquid. *Journal of Fluid Mechanics* 2005; **530**:369–378.
70. Gerlach D, Biswas G, Durst F, Kolobaric V. Quasi-static bubble formation on submerged orifices. *International Journal of Heat and Mass Transfer* 2005; **48**:425–438.
71. Buwa VV, Gerlach D, Durst F, Schlucker E. Numerical simulation of bubble formation on submerged orifices: period-1 and period-2 bubbling regimes. *Chemical Engineering Science* 2007; **62**:7119–7132.
72. Gerlach D, Alleborn N, Buwa V, Durst F. Numerical simulation of periodic bubble formation at submerged orifices under constant inflow conditions. *Chemical Engineering Science* 2007; **62**:2109–2125.
73. Zhang L, Shoji M. Aperiodic bubble formation from a submerged orifice. *Chemical Engineering Science* 2001; **56**:5371–5381.
74. McCann D, Prince R. Regimes of bubbling at a submerged orifice. *Chemical Engineering Science* 1971; **26**:1505–1512.
75. Taylor GI, The viscosity of a fluid containing small drops of another fluid. *Proceedings of the Royal Society London*, *Series A* 1932; **138**:41–48.
76. Bentley BJ, Leal LG. An experimental investigation of drop deformation and breakup in steady, two-dimensional linear flows. *Journal of Fluid Mechanics* 1986; **167**:241–283.
77. Loewenberg M, Hinch EJ. Numerical simulation of a concentrated emulsion in shear flow. *Journal of Fluid Mechanics* 1996; **321**:395–419.
78. Guido S, Simeone M, Greco F. Effects of matrix viscoelasticity on drop deformation in dilute polymer blends under slow shear flow. *Polymer* 2003; **44**:467–471.
79. Li J, Renardy YY, Renardy M. Numerical simulation of breakup of a viscous drop in simple shear flow through a volume-of-fluid method. *Physics of Fluids* 2000; **12**(2):269–282.
80. Renardy YY, Cristini V. Effect of inertia on drop breakup under shear. *Physics of Fluids* 2001; **13**(1):7–13.
81. Badalassi VE, Ceniceros HD, Banerjee S. Computation of multiphase systems with phase field models. *Journal of Computational Physics* 2003; **19**:371–397.
82. Hiller W, Kowalewski TA. An experimental study of the lateral migration of a droplet in a creeping flow. *Experiments in Fluids* 1987; **5**:43–48.
83. Shapira M, Haber S. Low Reynolds number motion of a droplet between two parallel plates. *International Journal of Multiphase Flow* 1988; **14**:483–506.
84. Couillette C, Pozrikidis C. Motion of an array of drops through a cylindrical tube. *Journal of Fluid Mechanics* 1998; **358**:1–28.
85. Olbricht WL. Pore-scale prototypes of multiphase flow in porous media. *Annual Review of Fluid Mechanics* 1996; **28**:187–213.
86. Mortazavi S, Tryggvason G. A numerical study of the motion of drops in Poiseuille flow. Part 1. Lateral migration of one drop. *Journal of Fluid Mechanics* 2000; **411**:325–350.
87. Keh HJ, Chen PY. Slow motion of droplet between two parallel plane walls. *Chemical Engineering Science* 2001; **56**:6863–6871.
88. Griggs AJ, Zinchenko AZ, Davis RH. Low Reynolds number motion of deformable drops between two parallel plane walls. *International Journal of Multiphase Flow* 2007; **33**:182–206.